Ceramics International 46 (2020) 2743–2757

Contents lists available at ScienceDirect

Ceramics International

journal homepage: www.elsevier.com/locate/ceramint

A reactive-sputter-deposited TiSiN nanocomposite coating for the protection of metallic bipolar plates in proton exchange membrane fuel cells

Shuang Peng[a], Jiang Xu[a,b,*], Zhengyang Li[c], Shuyun Jiang[d], Paul Munroe[e], Zong-Han Xie[f,g], Hong Lu[h]

[a] Department of Material Science and Engineering, Nanjing University of Aeronautics and Astronautics, 29 Yudao Street, Nanjing, 210016, PR China
[b] School of Mechanical & Electrical Engineering, Wuhan Institute of Technology, 693 Xiongchu Avenue, Wuhan, 430073, PR China
[c] Institute of Mechanics, Chinese Academy of Sciences, Beijing, 100190, PR China
[d] Department of Mechanical Engineering, Southeast University, 2 Si Pai Lou, Nanjing, 210096, PR China
[e] School of Materials Science and Engineering, UNSW Sydney, NSW, 2052, Australia
[f] School of Mechanical Engineering, University of Adelaide, SA, 5005, Australia
[g] School of Engineering, Edith Cowan University, Perth, WA, 6027, Australia
[h] Xin jiang Yihe Biology Co.,Ltd, Regiment headquarters of Crops 66, Cocodala, 835219, PR China

ARTICLE INFO

Keywords:
Proton exchange membrane fuel cell (PEMFC)
Bipolar plate
Titanium alloy
TiSiN coating
Corrosion resistance

ABSTRACT

To meet the needs of corrosion resistance and electrically conductivity for metallic bipolar plates that are employed in proton exchange membrane fuel cells (PEMFCs), a TiSiN nanocomposite coating was fabricated on to a Ti–6Al–4V substrate using reactive sputter-deposition through the double cathode glow discharge plasma technique. The microstructure of the TiSiN coating comprised nanocrystallite TiN grains embedded in an amorphous Si_3N_4 matrix. Electrochemical measurements were employed to investigate the corrosion behavior of the TiSiN coating in the simulated operating environments of a PEMFC, specifically 0.5 M H_2SO_4 solution containing different HF concentrations (namely 2, 4 and 6 ppm) at 70 °C pumped with H_2 at the anode and air at the cathode. With increasing HF concentration, a higher corrosion current density and lower corrosion potential were observed from both the coating and the uncoated substrate, indicating that the addition of HF accelerated their corrosion rates under these conditions. Compared to the uncoated substrate, the TiSiN coating showed a markedly higher corrosion resistance at all HF concentrations. The passive film that formed on the TiSiN coating, with a resistance of the order of magnitude of ~10^7 Ω cm^2, displayed good electrochemical stability and was less affected by changes in HF concentration. For the TiSiN coating, the values of interfacial contact resistance (ICR) were 14.7 mΩ cm^{-2} and 18.3 mΩ cm^{-2}, respectively, before and after 2.5 h potentiostatic polarization with 6 ppm HF under cathodic conditions under a compaction pressure of 140 N cm^{-2}. Both values are much lower than those for the bare substrate. Moreover, the TiSiN coating was shown to improve the hydrophobicity of Ti–6Al–4V that would help facilitate water management in the PEMFC operating environment. This coating, which exhibited excellent corrosion resistance, electro-conductivity and hydrophobicity, is therefore a promising material for protecting metallic bipolar plates from corrosive attack.

1. Introduction

To meet the ever increasing demands for clean energy, much attention has been devoted to fuel cells that convert chemical energy into electricity without the generation of pollution and mechanical noise [1]. Amongst the different types of fuel cells available, the proton exchange membrane fuel cell (PEMFC) exhibits commercial potential for applications in electric vehicles and portable power. This is brought about mainly by its unique operating capabilities, including high-power density, low-emission, fast start-up and low temperature of operation [2–4]. As the biggest contributor to the weight and cost of PEMFC stacks, bipolar plates are capable of performing several key functions in the fuel cell, including providing structural support for the cell stack, separating and distributing fuel gas and oxygen over the active areas of the cells, facilitating management water and heat generated and conducting electric currents from cell to cell [5,6]. In the PEMFC stacks, the

* Corresponding author. Department of Material Science and Engineering, Nanjing University of Aeronautics and Astronautics, 29 Yudao Street, Nanjing, 210016, PR China.
E-mail address: xujiang73@nuaa.edu.cn (J. Xu).

https://doi.org/10.1016/j.ceramint.2019.09.263
Received 31 July 2019; Received in revised form 25 September 2019; Accepted 26 September 2019
Available online 27 September 2019

bipolar plates are always in contact with the gas diffusion layer (GDL)/membrane electrode assembly (MEA). When the PEMFC system is running, these bipolar plates are exposed to a hostile operating environment containing anions such as SO_4^{2-}, HSO_4^-, HCO_3^- and F^-, etc., which originate from the dissolution of membrane and the MEA [7].

Candidate materials for bipolar plates should have good electrical conductivity to minimize electrical losses, high corrosion resistance to reduce the chemical damage to the proton exchange membrane during operation and good hydrophobicity to eliminate redundant water presented in the PEMFC stack [8,9]. In terms of chemical stability and electrical conductivity graphite-based composites have been commonly used for the current generation of bipolar plates. However, such materials present several demerits including high manufacturing cost, inadequate mechanical strength and relatively high gas permeability [10]. To address these problems, metallic bipolar plates made from, for example, stainless steel or Ti, Al and Ni based alloys, have been considered [11–14]. Among them, Ti alloys offer many advantages over other alloys since they exhibit higher specific strength and superior chemical stability in highly acidic environments [12].

Unfortunately, metallic bipolar plate materials are affected by surface electrochemical corrosion under the harsh acidic and humid operating conditions of the PEMFC [7]. Chemical attack of metallic bipolar plates often releases metal cations and the formation of a passive oxide layer, poses a challenge for commercial application. For example, the dissolved metal ions, especially at the anode, can diffuse to proton exchange sites, which poison the catalysts in the MEA and reduce proton transfer rate, thereby degrading long-term membrane performance [15,16]. On the other hand, although passive oxide films may retard corrosion of metallic bipolar plates, these non-conductive films may increase the interfacial contact resistance between the bipolar plate and the adjacent graphite electrode backing layer, thereby increasing potential loss [17]. Therefore, the surface characteristics of metallic bipolar plates are critical for improving the performance of a PEMFC.

To resolve issues pertaining to corrosion and contact resistance, many attempts have been made by employing a range of diverse surface modification techniques to develop robust coatings to combat surface degradation in corrosive PEMFC's environments [18]. As such, coated metallic bipolar plates can be designed to take advantage of the combination of the merits of both metal substrate and the inert, yet electrically conductive, coating. As a common transition metal nitride, TiN has been extensively applied as a hard and protective coating to improve the working performance of cutting tools and mechanical parts. This is because of its attractive mix of properties such as good hardness, high temperature oxidation resistance and wear resistance [19–21]. As such, TiN is a candidate coating material for protection of metallic bipolar plates, owing to its good corrosion resistance and metal-like conductivity [22]. Zhang et al. [23] evaluated the feasibility of TiN coatings, prepared through a multi-arc ion plating technique, onto a Ti substrate as bipolar plate. Fuel cell testing indicated that the maximum power density of a cell using TiN-coated Ti bipolar plate was 0.68 W cm^{-2} at a current density of 1600 mA cm^{-2}, superior to that of an uncoated titanium bipolar plate. However, to cope with the harsh environment of the PEMFC, more efforts have focused on the behavior of multicomponent TiN-based coatings through incorporation of elements such as Al, Cr, O and Si [24–27]. Lin et al. [28] found that the corrosion resistance of a (Ti,Zr)N nano-composite coating outperformed that of compounds such as TiC, TiN and ZrN and improved the corrosion resistance of uncoated 304s stainless steel bipolar plates or uncoated Ti bipolar plates by over 200 times. Kim et al. [29] investigated the corrosion resistance of the TiN_xO_y films under PEMFC simulated conditions. They showed that the corrosion current density of the TiN_xO_y films (2.7×10^{-6} A cm^{-2}) at a fixed potential of 0.6 V $_{SCE}$ is much lower than that compared with binary TiN (8×10^{-6} A cm^{-2}). They assumed that the presence of oxygen in the TiN_xO_y films, located at the columnar grain boundaries, acted to inhibit corrosive media from penetrating to the substrate.

It should be noted, however, that the TiN based coatings fabricated by PVD and CVD methods often have inherent microstructural defects, such as pinholes, micro-cracks and macro-particles. These defects are detrimental to coating durability under PEMFC conditions, because the penetration of anions in the electrolyte through innate defects results in corrosive attack on the underlying substrate. However, recently, double cathode glow discharge plasma technique was used to prepare engineering coatings free of these defects [30,31]. This is, in part, linked to the higher deposition temperatures employed in this method, which increases the mobility of deposited atoms and also helps over the self-shadowing effects exerted by previously deposited atoms, thereby effectively decreasing the number of defects.

The addition of Si to TiN coatings, where Si replaces Ti, which promotes the formation of an amorphous nitride, is known to be a suitable way to optimize this material's surface chemical and mechanical properties. However, up to now, the application of ternary TiSiN as a protective nanocomposite coating for metallic bipolar plates has not been investigated. Nevertheless, concerns remain over the release of fluoride ions in the form of HF from fluorinated membranes, which facilitates the initiation of corrosion of the metallic bipolar plates. In this work, a reactive sputtered TiSiN nanocomposite coating was deposited on to a Ti–6Al–4V substrate using a double cathode glow discharge plasma technique. The electrochemical corrosion behavior of the TiSiN nanocomposite coating was investigated in a simulated PEMFC environment, with different HF concentrations in an effort to understand the improvements possible in the corrosion resistance of titanium alloy bipolar plates. In addition, the interfacial contact resistance and contact angle of the TiSiN nanocomposite coating were also measured and compared with uncoated Ti–6Al–4V.

2. Experimental procedure

2.1. Sample preparation

The TiSiN coating was deposited on a Ti–6Al–4V substrate by reactive sputter-deposition technique called double cathode glow discharge plasma. In this process, the target and the substrate act as the two cathodes, respectively. Details of the method are described in detail elsewhere [32]. The substrate was cut into discs, ~3 mm in thickness, from a titanium alloy rod (the nominal composition used here (in wt%) was: Al, 6.42; V, 4.19; Fe, 0.198; O, 0.101; C, 0.011; N, 0.006 and the balance, Ti.) with a disc diameter of ~30 mm. The substrate was ground to a fine surface finish (R_a) of 0.2 μm. It was then subject to cleaning, using acetone, then alcohol and, finally, distilled water and then dried before the deposition. The sputtering target was prepared from a mixture of ball-milled Ti powder (300 mesh, > 99.9% purity) and Si powder (200 mesh, > 99.9% purity) with ratio of 86 at.% and 14 at.%, respectively, was pressed into a disk shape with dimensions Φ80 × 4 mm by cold compaction using an applied pressure of 600 MPa. The applied voltages on the target and substrate were −900 V and −300 V, respectively, with a 10 mm distance between them. The deposition temperature was monitored via a thermocouple located near the sample. For this experiment the substrate was held at 600 ± 20 °C. The pressure in the chamber during the deposition process was maintained at 35 Pa consisting of a mixture of Ar/N_2. The $Ar:N_2$ flux ratio was held at 10:1. For this coating, the deposition time was 3 h and the deposition rate is ~3.5 μm/h, such that a coating of ~10 μm thick was formed.

2.2. Structural characterization

The phase composition of the coating was analyzed by X-ray diffraction (XRD) using D8 ADVANCE with a Cu-Kα radiation, operating at 40 mA and 35 kV. The 2θ scan range used was from 20° to 90° using a

scan rate of 10°/min. A grazing incidence angle of 2° was used to minimize any interference effects from the substrate.

The coating cross-section and sample surface following corrosion testing were examined using a Fei Quanta200 scanning electron microscope (SEM). The composition of the coating was investigated through energy dispersive spectroscopy (EDS) analysis. Higher resolution analysis was performed by a JEOL2100 transmission electron microscope (TEM) operating at a 200 kV accelerating voltage. Plan-view TEM specimens were prepared by slicing thin sections, mechanical grinding, dimpling and finally electropolishing from the uncoated side of the sample. Cross-sectional TEM samples were sectioned using a dual beam focused ion-beam (FIB) microscope (Nova Nanolab 200, FEI, Hillsboro, Oregon, USA).

The chemical states of the elements on the surface of the coating, both before and after corrosion, were investigated using X-ray photoelectron spectroscopy (XPS). The instrument used was a Kratos AXIS Ultra ESCA System. A monochromatic Al K_α X-ray source ($h\nu$ = 1486.68 eV) with an emission current of 12 mA and an applied voltage of 12 kV was used. For the survey scans, the pass energy was set at 100 eV, and 20 eV was used for feature scans to acquire the high-resolution spectra. A base pressure of $\sim 10^{-10}$ Torr was maintained in the sample analysis chamber during acquisition. The Shirley background, Gaussian and mixed Gaussian/Lorentzian functions with least-square routines were used for spectra fitting of the data. The C1s binding energy peak at 285 eV, arising from hydrocarbon contamination, was used to calibrate the spectral positions. Peaks were identified with reference to the NIST XPS database (V4.0).

2.3. Nanoindentation and scratch testing

The hardness and the modulus of the as-deposited coating and the bare titanium alloy substrate were evaluated through nanoindentation testing. A Berkovich diamond tip, with a radius of 5 µm, was employed. Before testing fused silica was employed as a standard for calibration of the tip. In order to reduce substrate effects, the maximum load applied by nanoindentation was 20 mN. The tip was pressed into the surface of the samples at a loading rate of 40 mN/min. The hardness and elastic modulus of each set of specimens were calculated from at least five sets of indentation data through the Oliver and Pharr method [33].

To determine the adhesion behaviour between the TiSiN coating and the substrate scratch testing using a CSM REVETEST (CSM Instruments, Switzerland) scratch tester equipped with a diamond stylus with a tip radius of 200 µm. A progressive load from 0 N to 100 N was applied to the stylus at a loading rate of 12.5 N/min. The scratch track length was set to be 8 mm and the scratch speed was 8 mm/min. The frictional force and penetration depth, as a function of normal force, were recorded simultaneously.

2.4. Electrochemical measurements

Electrochemical measurements were recorded with a CHI660C workstation (Shanghai ChenHua Instruments Inc., China). A standard three-electrode cell configuration, consisting of the test sample, as a working electrode with an exposed area of 1.0 cm^2, a saturated calomel electrode (SCE), as reference (all electrode potentials in this paper were referred to the SCE), and a sheet of platinum as a counter electrode, was used for the electrochemical experiments. To simulate the hostile environment in the PEMFC, a solution was made up of 0.5 M H_2SO_4 with differing HF concentrations (specifically, 2, 4 and 6 ppm) that were used at a temperature of 70 °C. In addition, H_2 was pumped to simulate the anodic operating PEMFC environment and, similarly, air was supplied for the cathodic condition. The open-circuit potential test was carried out after 10 min of depolarization and lasted 1 h. For the potentiodynamic polarization measurements, the voltage sweep rate was 20 $mVmin^{-1}$. For the potentiostatic polarization measurements, the applied potential was −0.1 V_{SCE} and +0.6 V_{SCE} for the anode and cathode, respectively. A test time of 2.5 h was used. For electrochemical impedance spectroscopy (EIS) tests, the frequency sweep ranged from 10^5 Hz to 10^{-2} Hz with a sinusoidal voltage of 10 mV and 12 steps were divided for each decade of frequency.

2.5. Interfacial contact resistance (ICR) and contact angle measurements

The ICR between the surface of the sample and a gas diffusion layer (GDL) was determined; details have been described elsewhere [34]. During the experiment, the sample was placed between two pieces of conductive carbon paper (Toray TGP-H-090), which were sandwiched between two plates of Au-coated copper plates. The applied current was stabilized at 5A with the compaction force on the two Au-coated copper plates gradually increasing from 20 to 260 Ncm^{-2}. The corresponding total voltage was recorded to calculate the total resistance as a function of compaction force. The resistance of the carbon paper that was sandwiched between two Au-coated copper plates was measured in the same way and that was subsequently subtracted from the total resistance. Further, the ICR of the TiSiN coated and uncoated Ti–6Al–4V before, and after, 2.5 h potentiostatic polarization at the cathode condition in a 0.5 M H_2SO_4 + 6 ppm HF solution, was measured to determine the effect of corrosion on the interfacial contact resistance.

The contact angles of the coated and uncoated substrate were measured to evaluate hydrophobicity. The sessile drop method was employed using a Hamilton syringe to produce water drops at room temperature. A contact-angle meter (JC2000C, POWEREACH) was used to evaluate the contact angle of the droplet. Average values were obtained from at least 3 experiments.

3. Results and discussion

3.1. Phase identification and microstructural analysis

Fig. 1 shows a typical X-ray diffraction (XRD) spectrum for the TiSiN coated Ti–6Al–4V substrate. From this XRD spectrum, it can be seen that three main diffraction peaks centered around 2θ values of 36.3° , 42.6° and 61.7° are present that can, respectively, be assigned to the (111), (200) and (220) crystallographic planes, respectively, of cubic B1 NaCl-type structured TiN. Compared with the standard powder XRD data, recorded in the JCPDS card (No.38–1420, marked by vertical lines in Fig. 1), the addition of Si shifts the characteristic peaks slightly towards lower 2θ values. Further, there is an absence of peaks associated with crystalline phases of silicon nitride or titanium silicide, suggesting that the incorporated Si is present as either a TiN solid solution or as an amorphous phase. This is also in agreement with observations reported elsewhere [35]. The peaks in the spectra were broad and with low intensity suggesting the presence of very fine grains in the TiSiN coating. XRD peak broadening analysis was used to estimate the mean mono-

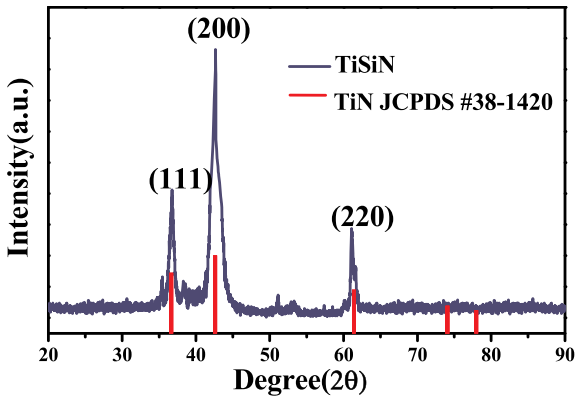

Fig. 1. Typical X-ray diffraction pattern recorded from the as-deposited TiSiN coating.

Table 1
The calculated grain sizes of TiN based on the (1 1 1), (2 0 0) and (2 2 0) planes and the texture coefficient for the crystallographic planes in the TiSiN coating.

Crystal plane	(111)	(200)	(220)
D (nm)	7.4	6.7	6.3
TC_{hkl}	0.83	1.35	0.86

crystalline size in a direction perpendicular to the diffracting lattice plane, using Scherrer's formula

$$D_{hkl} = \frac{K\lambda}{\beta cos\theta} \quad (1)$$

where D_{hkl} is average crystallite size, β is the corrected width at half-height of its maximum intensity, θ is the Bragg angle, λ is the X-ray wavelength (0.154 nm for Cu K_α radiation), K is a dimensionless shape factor (0.94). As shown in Table 1, the average crystallite sizes calculated from the (111), (200) and (220) lines were estimated to be 7.4, 6.7 and 6.3 nm, respectively.

For coatings prepared by sputter-deposition technologies, preferred growth orientation is commonly observed. To gain insight into the preferred orientation of the crystal planes for this coating, the texture coefficients were calculated to compare the relative intensities of the observed diffraction peaks. The texture coefficient (TC_{hkl}) describes the texture intensity generated by grains oriented in a given (hkl) reflection and can be determined from the normalized XRD peaks by using the following formula [36]:

$$TC_{hkl} = \frac{I_m(hkl)/I_0(hkl)}{\frac{1}{n}\sum_1^n I_m(hkl)/I_0(hkl)} \quad (2)$$

where, for a given (hkl) reflection, I_m(hkl) and I_0(hkl) represent the peak intensity from the TiSiN coating and a standard reference sample, respectively; n is the total number of diffraction peaks used in the calculation. When the $TC_{(hkl)}$ ranges from 0 to 1, preferred crystal growth along a given crystallographic direction is restrained; while when $TC_{(hkl)} > 1$ a preferential orientation of crystal growth along a given crystallographic direction is indicated. It can be seen from Table 1 that the TiSiN coating exhibits a preferential growth along the [200] crystallographic direction. The evolution of preferred orientation in the TiSiN nanocomposite coating arises from minimizing the overall Gibbs free energy of the coating, composed of surface and strain energy [37]. For the NaCl-type structured TiN, the (111) preferred orientation occurs under high stress conditions, where strain energy is the dominant contribution to the total free energy, while the (200) preferred orientation is favored under low stress conditions in which the surface energy contribution is the dominant [38]. Therefore, the competition between surface energy and strain energy controls the preferred grain growth in the coating. Several researchers have suggested that the growth stress during coating deposition is lower at a higher deposition temperature [39,40]. This is consistent with the (200) preferred orientation observed here, presumably due to the relatively high deposition temperature employed.

Surface chemical bonding status and elemental concentrations of the TiSiN coating were determined by XPS. Before examination, the coating surface was etched with a 1 keV Ar^+ ion beam for 3 min to remove any surface contamination. From the XPS full spectrum of the coating (Fig. 2), peaks from Ti 2p, Si 2p, N 1s and C 1s are observed, among which a negligible C 1s peak can be observed resulting from hydrocarbon contaminant covering the sample surface. According to the results of elemental quantification calculated from the areas of the Ti 2p, Si 2p and N 1s XPS peaks, the composition of the TiSiN nanocomposite coating can be expressed in the form $Ti_{44}Si_7N_{49}$. From the core–electron level Ti 2p spectrum (Fig. 2(b)), a doublet with Ti $2p_{3/2}$ and Ti $2p_{1/2}$ peaks located at 454.8 and 460.6 eV, with a spin orbit splitting of 5.8 eV, is identified as from Ti–N bonds in TiN [54]. From Fig. 2(c), it is found that the N1s peak can be deconvoluted into an intense peak at 397.06 eV and a weak shoulder peak at 398.8 eV, which are attributable to the N–Ti bonds in TiN [41] and the N–Si bonds in amorphous Si_3N_4 [42], respectively. From quantitation of the N1s spectrum, the phase fractions for the TiSiN nanocomposite coating can be obtained as. 96.2% TiN and 3.8% Si_3N_4, respectively. The Si 2p signal (Fig. 2(d)) was observed as a symmetric single peak at a binding energy of 101.5 eV, in good agreement with the value for stoichiometric Si_3N_4 [48]. No evidence for Si–Si bonds (at 99.2 eV) and Si–Ti bonds (at 98.4 eV) were detected [43], suggesting a high ionization rate of nitrogen gas during deposition.

Fig. 3(a) is a typical cross-sectional secondary electron micrograph of the coating that exhibits a distinct contrast difference between the coating and substrate. The TiSiN nanocomposite coating, with an average thickness of ~10 μm, appears to exhibit a brighter contrast, showing a homogeneous and compact structure, free of defects, such as voids or pinholes, across the entire coating thickness or at the coating/substrate interface. The interface between the coating and the substrate exhibits a smooth transition with strong metallurgical bonding. As mentioned above, the anions present in the PEMFC operating environment can penetrate into the coating through such defects, resulting in the electrochemical reactions at the interface between the coating and substrate. Thus, the dense microstructure of this coating can act as a barrier layer to impede the transport of electrons and ions between the electrolyte and substrate, thereby reducing the electrochemical reaction rate. EDS microanalysis (Fig. 3(b)) revealed that the composition of alloy elements is broadly in accordance with the result of XPS analysis.

As shown in Fig. 4 (a) and (b), the plan-view bright-/dark-field TEM images and a cross-sectional bright field TEM images, respectively, show that the microstructure of the TiSiN coating is characterized by a homogeneous distribution of equiaxed grains. The size of these grains ranges from 4 to 18 nm, with a mean grain size of ~10 nm, determined from the statistical analysis of the grain size distribution (Fig. 4 (c)). Compared to the calculated grain size obtained from the XRD data, the measured mean grain size is slightly larger, due to the presence of structural defects and the disordered nature of the grain boundaries [44]. From the selected area electron diffraction (inset in Fig. 4(b)), it is observed that there are three clear diffraction rings representing the (111), (200) and (220) reflections for cubic B1 NaCl-type structured TiN. The (200) ring exhibited the highest diffracted intensity providing further evidence that the (200) plane is the preferred orientation. A bright-field HRTEM image (Fig. 4(d)) shows the nanocrystalline lattices of TiN that are embedded in an amorphous matrix, which is identical with that previously reported in the literature [45]. As evident in Fig. 4 (e), which shows a cross-sectional TEM bright-field image, the coating exhibits a granular morphology with no evidence of the columnar structure that is typical for TiN-based coatings.

3.2. Nanoindentation and scratch testing

Fig. 5 shows the typical load-displacement curves for the TiSiN coating and the bare Ti–6Al–4V substrate at a maximum load of 20 mN. It is clear that the TiSiN coated sample exhibits a higher resistance to local deformation with a smaller maximum penetration depth and residual indentation depth compared with the uncoated substrate. The hardness and the elastic modulus of the specimens were determined from the indentation data through the Oliver and Pharr method. The presence of the TiSiN coating increases the hardness (H) from 6.3 ± 0.83 GPa to 35.9 ± 2.1 GPa and the elastic modulus (E) from 146.6 ± 6.8 GPa to 380.7 ± 9.2 GPa, respectively. As reported elsewhere, the microstructure, hence hardness and elastic modulus, of TiSiN coatings are significantly affected by silicon concentration [46]. Coatings with a Si content of less than 4 at.% exhibit columnar grains rather than a nanocomposite structure [47]. Moreover, Si contents exceeding 9 at.% leads to increases in the thickness of the amorphous

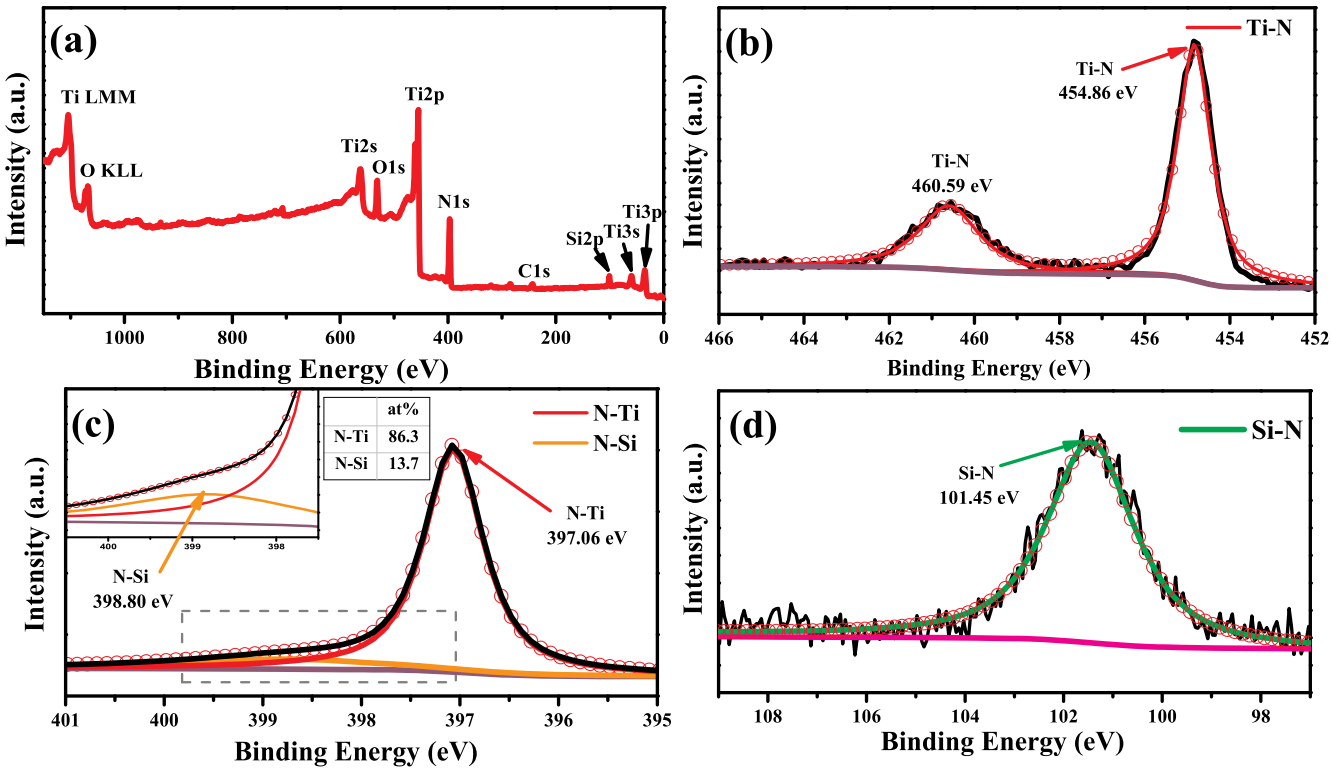

Fig. 2. (a) XPS survey spectra and the high-resolution XPS spectra for Ti 2p (b), Si 2p (c) and N1s (d) peaks collected from the TiSiN coated sample.

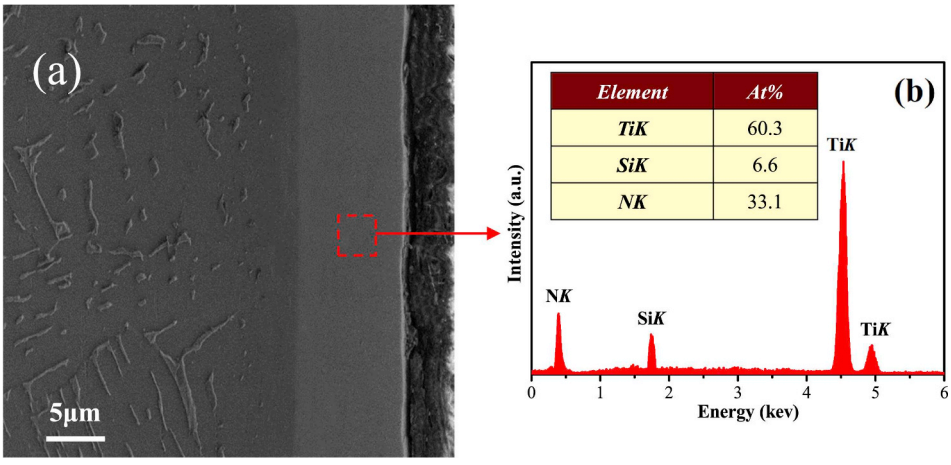

Fig. 3. Typical cross-sectional SEM micrograph (a) and corresponding EDS spectrum (b) for the TiSiN coating.

intergranular Si_3N_4 phase [48]. In both cases this. leads to a reduction in hardness and elastic modulus for TiSiN coatings. Therefore, the Si content of the as-deposited TiSiN coating (determined to be ~7 at.%) in this study is appropriate to maximize the hardness of the coating.

Under contact deformation, the intrinsic strength of the coating and the bonding strength between the deposited coating and underlying substrate are in competition. Interfacial delamination is more likely to occur in hard coatings due to their high intrinsic strength [49,50]. Thus, the adhesion strength between the TiSiN coating and the substrate should be investigated to evaluate the performance and reliability of TiSiN coated bipolar plates. Fig. 6(a) shows the frictional force and penetration depth as a function of applied load in a scratch test performed on the TiSiN coating. For progressive load scratch tests, two critical loads are used as measures of coating adhesive strength, i.e. L_{C1} and L_{C2}. L_{C1} represents the load where the initial failure event of the coating occurs, and L_{C2} is defined as the load where complete failure occurs leading to exposure of the substrate. As observed from Fig. 6(a), L_{C2} was determined to occur at a normal load of 59 N, where a sudden increase in the frictional force and the penetration depth occurred. This was confirmed by SEM analysis of the scratch track (shown in Fig. 6 (b) and (d)), where the TiSiN coating completely peeled away (adhesive spalling) resulting in substrate exposure at the corresponding position. Before the load reached L_{C2}, some parallel stripes, regarded as resulting from plastic deformation, were observed perpendicular to the scratch direction in the groove of the scratch track. The discontinuous chips (cohesive chipping) present at the rim of the scratch track are also considered to be failure events [51,52]. It is difficult to detect the initial failure at L_{C1} from the frictional force or penetration depth plots. However, according to observations of the scratch track surface morphology at the lower normal load, the initial chipping of the TiSiN coating (shown in Fig. 6(c)) occurred at a normal load of 47 N which is identified as L_{C1}. In general, coatings exhibiting a critical load over 30 N

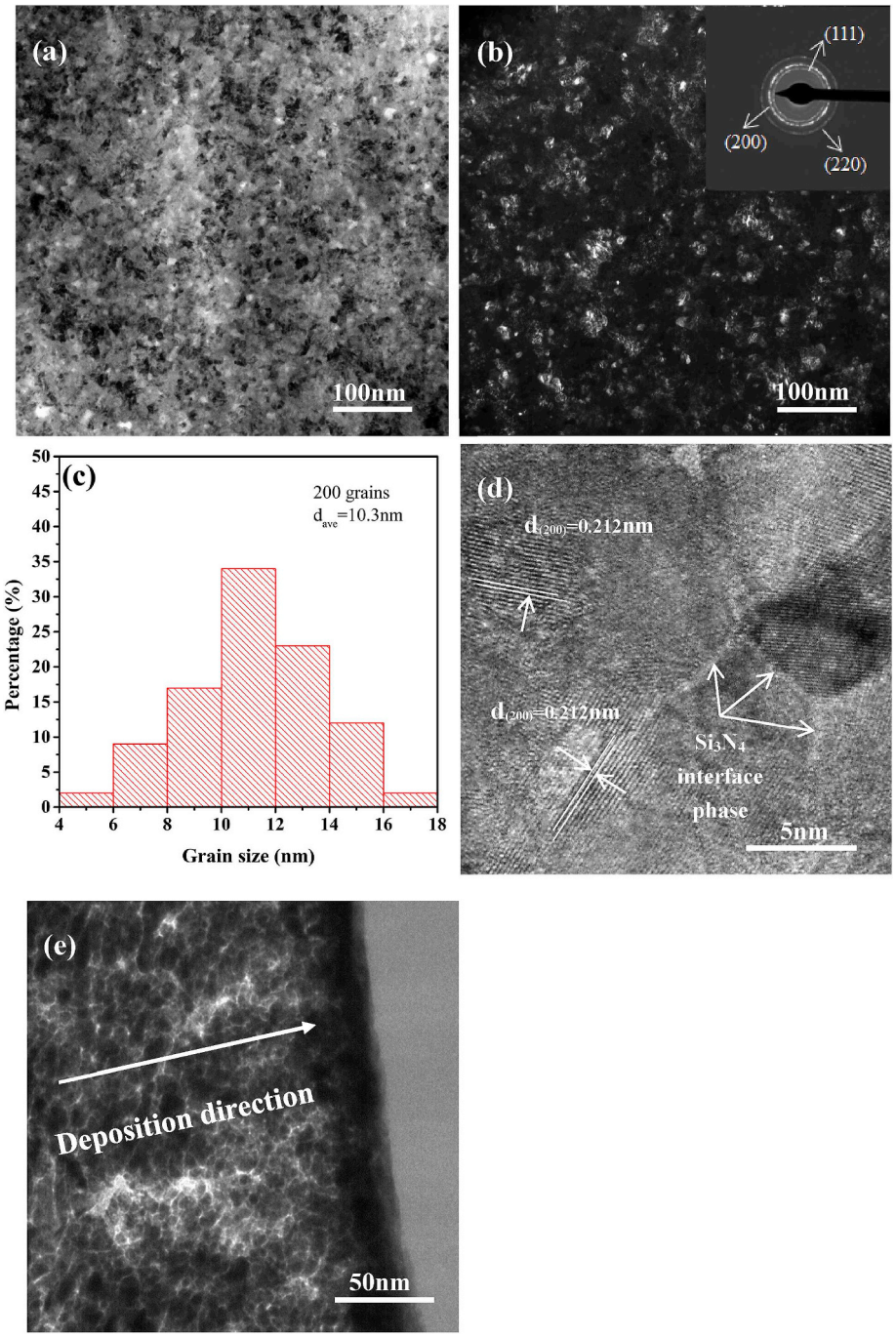

Fig. 4. Typical plan-view TEM bright-field (a) and dark-field (b) images of the TiSiN coating with the corresponding SAD pattern inset. (c) The statistical histogram of the grain sizes in TiSiN coating. (d) A high-resolution electron microscopy (HRTEM) image of the TiSiN coating. (e) Cross-sectional TEM bright-field image of the TiSiN coating.

are sufficient for sliding contact applications [53]. Thus, the TiSiN coating exhibited good adhesion strength and scratch resistance adequate to survive superficial damage during transit and assembling processes.

3.3. Electrochemical analysis

3.3.1. Open circuit potentials

The variation of open circuit potential (E_{OCP}) over a period of 60 min for the TiSiN coating and the uncoated titanium substrate exposed to 0.5 M H_2SO_4 solutions, with differing HF concentrations, at 70 °C are presented in Fig. 7. This shows that the E_{OCP} values of both specimens exhibit a rapid drift in the positive direction until reaching constant values. The increase in the E_{OCP} values at the initial stage is related to the spontaneous formation of protective oxide films on the specimen surface. With increasing HF concentration, the E_{OCP} values of both specimens shift towards more negative values indicating an increasing tendency towards corrosion for the surfaces of both specimens [54]. This is because the TiO_2 and Ti_2O_3 present in these oxide films have been demonstrated to be dissolved by HF [55]. However, under the same HF concentration, the E_{OCP} values of the TiSiN coating are more positive than that for the Ti–6Al–4V substrate, revealing that the oxide films formed on the TiSiN coating exhibit more stability in HF containing acidic solutions compared with the bare substrate.

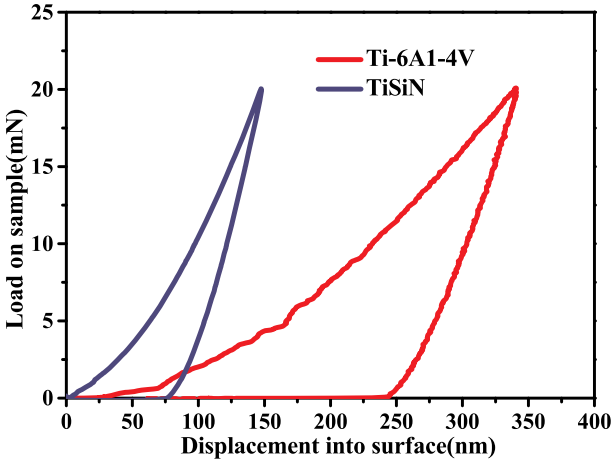

Fig. 5. Load–displacement curves of the as-deposited TiSiN coating and bare Ti-6A1-4 V substrate.

3.3.2. Potentiodynamic polarization studies

The potentiodynamic polarization curves of the TiSiN coating and the uncoated substrate in simulated anodic (pumped with H_2) and cathodic (pumped with air) PEMFC environments with different HF concentrations are shown in Fig. 8 (a) and (b), respectively. These data show clear differences in the shapes of the anodic branches between the two specimens. The TiSiN coated sample exhibits chemical inertness, with a wide potential plateau presented in the anodic branch, where the current density is independent of the potential. However, the uncoated Ti–6Al–4V substrate displays narrower passivation region and trans-passivation behaviour in the anodic branch exhibiting poor passivation capability. The electrochemical parameters (that is, corrosion potential (E_{corr}), corrosion current density (i_{corr}), anodic Tafel slope (β_a) and cathodic Tafel slope (β_c)), obtained from these curves through the Tafel extrapolation method [56], are summarized in Table 2. The protective efficiency (P_e) of the coating and the current densities at the operating potential ($i_{0.6V}$ or $i_{-0.1V}$) in both anodic and cathodic conditions are also given in Table 2. When the HF concentration increased from 2 ppm to 6 ppm, or the environment transformed from anodic to cathodic, both the coated and uncoated substrates display an increase in i_{corr} and a decrease in E_{corr}. This indicates that increasing the concentration of HF or dissolved oxygen in the solution can accelerate the rate of the corrosion reactions taking place on the surface of both two specimens. Nevertheless, under the same conditions, the TiSiN coating shows a higher i_{corr} and a more negative E_{corr} compared with the uncoated Ti–6Al–4V. Moreover, the current densities of the TiSiN coating are nearly three orders magnitude and four orders magnitude lower, respectively, than that of the bare substrate at the operating potential in anodic and cathodic conditions. This indicates that the TiSiN coatings reduce the corrosion rate and offer efficient protection for the titanium alloy substrate. The protective efficiency (P_e) of the TiSiN coating can be derived using the following equation [57]:

$$P_e(\%) = [1 - (\frac{i_{0.6V}}{i^0_{0.6V}})] \times 100 \quad (3)$$

where $i_{0.6V}$ and $i^0_{0.6V}$ are the current densities at the operating potential

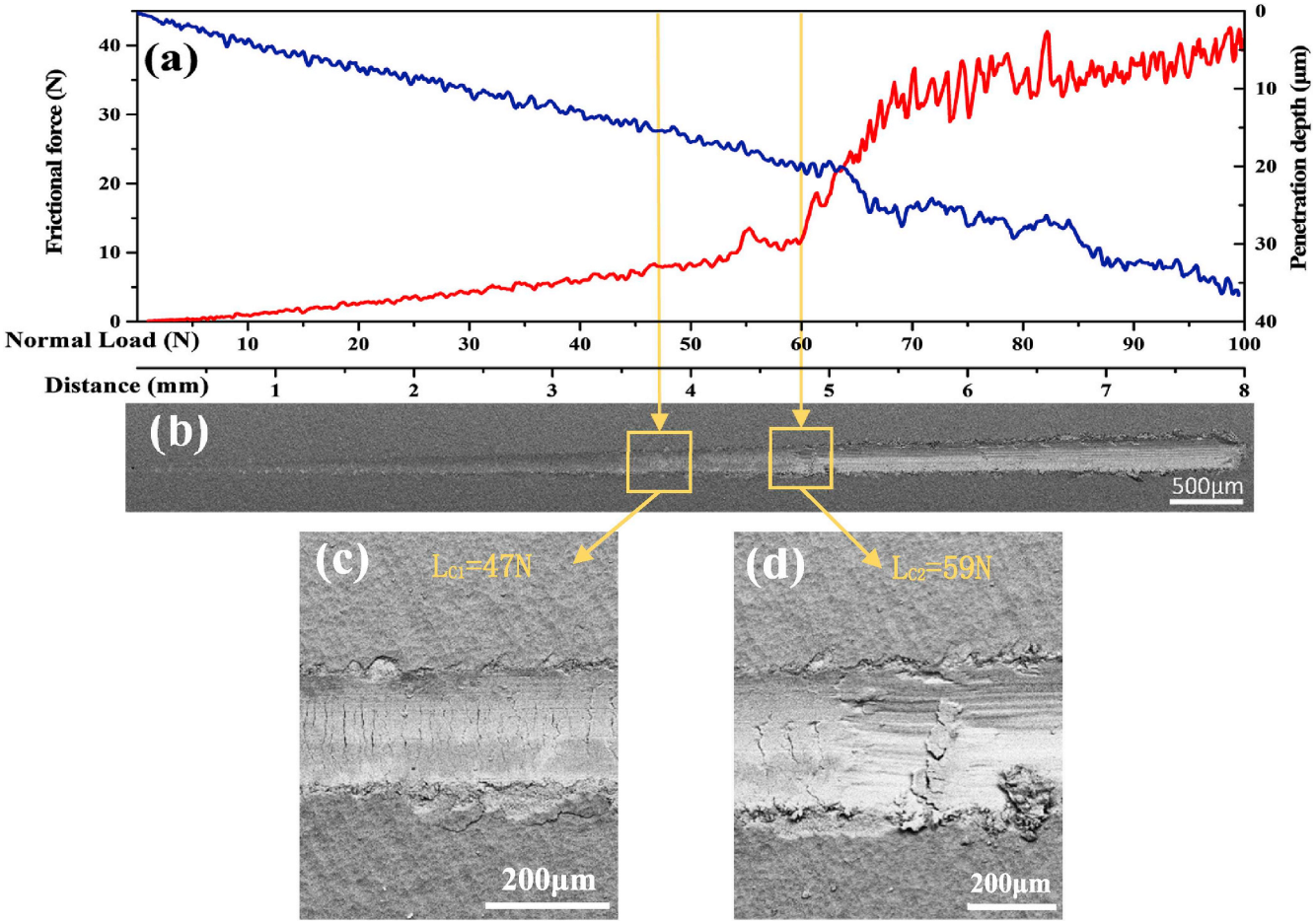

Fig. 6. Curve showing the frictional force and penetration depth as a function of normal force (a); secondary electron micrographs of the entire scratch track (b) and the surface morphology of the scratch track when the normal force reached L_{C1}(c) and L_{C2}(d).

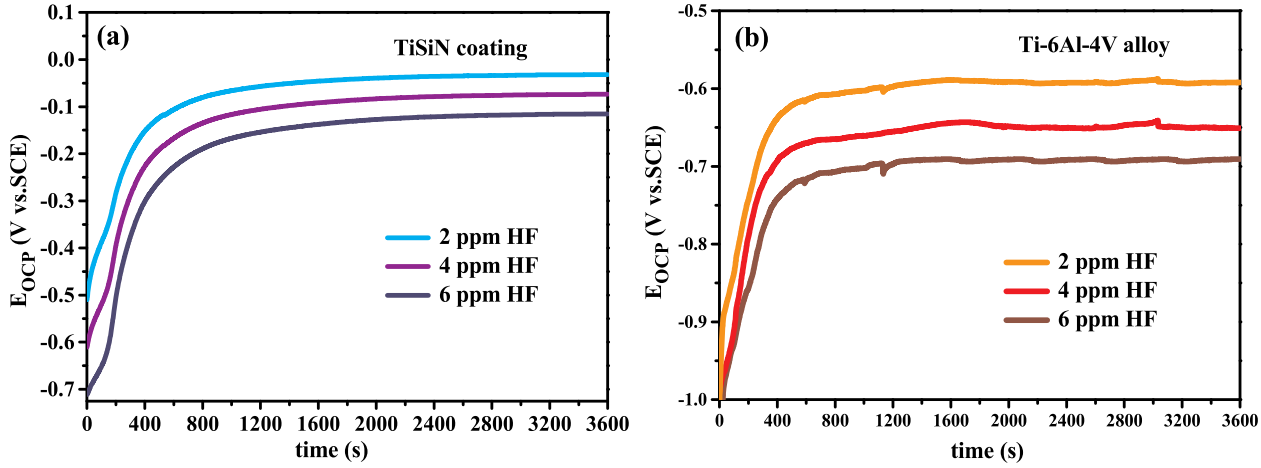

Fig. 7. The open circuit potential (E_{OCP}) values as a function of immersion time for the as-deposited TiSiN coating (a) and uncoated Ti-6A1-4 V (b) in 0.5 M H_2SO_4 solution with different concentrations of HF (namely, 2,4 and 6 ppm) at 70 °C.

in cathodic condition for the TiSiN coating and uncoated Ti–6Al–4V, respectively. As shown in Table 2, the values of the protective efficiency are above 99% for all conditions. It is worth noting that the P_e increases with increasing HF concentration. This may be because the corrosion resistance of the Ti–6Al–4V substrate deteriorates more severely than that for the TiSiN coating with increasing HF concentration.

Evans' diagrams were applied to give a theoretical explanation for the influence of the gas pumped into the solution (shown in Fig. 9 (a)) and the effect of variations in HF concentration (shown in Fig. 9 (b)) on the corrosion system. During the polarization process, the corrosion reactions consist of a number of local oxidation reactions and local reduction reactions. With the applied potential lower than E_{corr}, the reduction of H^+ ($2H^+ + 2e^- \rightarrow H_2$) and O_2 ($O_2 + 2H_2O + 4e^- \rightarrow 4OH^-$) are the dominant reactions on the work electrode. With the applied potential beyond E_{corr}, the oxidation and dissolution of the metal atoms at the surface of the TiSiN coating or uncoated Ti–6Al–4V are the dominant reactions on the work electrode. The theoretical current densities for the reduction of H^+ and O_2 as a function of applied potential can be calculated according to Ref. [58], and the total current densities of the oxidation reactions can be plotted according to the experimental data.

For a given HF concentration of 2 ppm, the current density of the oxidation reactions and reduction reactions as a function of applied potential supplied under the anodic and cathodic conditions are shown in Fig. 9 (a). With air pumped into the solutions, the O_2 reduction curve displays a shift towards the region with a higher current density and lower potential (i.e. the top left of the diagram in Fig. 9 (a)), but the H^+ reduction curve exhibits little difference. From the mixed potential theory, the values for E_{corr} and i_{corr} can be defined by the intersection of the total reduction curve and the total oxidation curve [59]. As can be seen from Fig. 9 (a), pumping air results in the intersection for the uncoated substrate shifting from point A to point B, indicating an increase in the values of E_{corr} and i_{corr} for the uncoated alloy. However, there is little shift of the intersection point, D, for the TiSiN coating. Moreover, pumping air also accelerates the oxidation reactions and thus increases the current density on the anodic branches in Tafel curves for both specimens, which leads to the intersection of the uncoated Ti–6Al–4V moving from point B to C and the intersection of the TiSiN coating moving from point D to E. Therefore, the TiSiN coating exhibits a smaller increment in corrosion rate than the bare substrate as it is only affected by oxidation reactions under the cathodic condition.

Under the cathodic condition (i.e. pumping air), the current density of the oxidation reactions and reduction reactions as a function of applied potential with different HF concentration are shown in Fig. 9 (b). With respect to reduction reactions, the HF concentration has little effect on the reduction curves due to the low degree ionization of HF and thus little contribution to the H^+ concentration. With respect to the oxidation reactions, as presented in Fig. 9 (b), the total oxidation curves exhibit a linear characteristic in the absence of any passive layers [60,61]. Further, the oxidation reactions are inhibited, due to barrier effects derived from the passive layers, which exhibits a non-linear oxidation curve with an increase in the value of β_a [62]. Therefore, at a

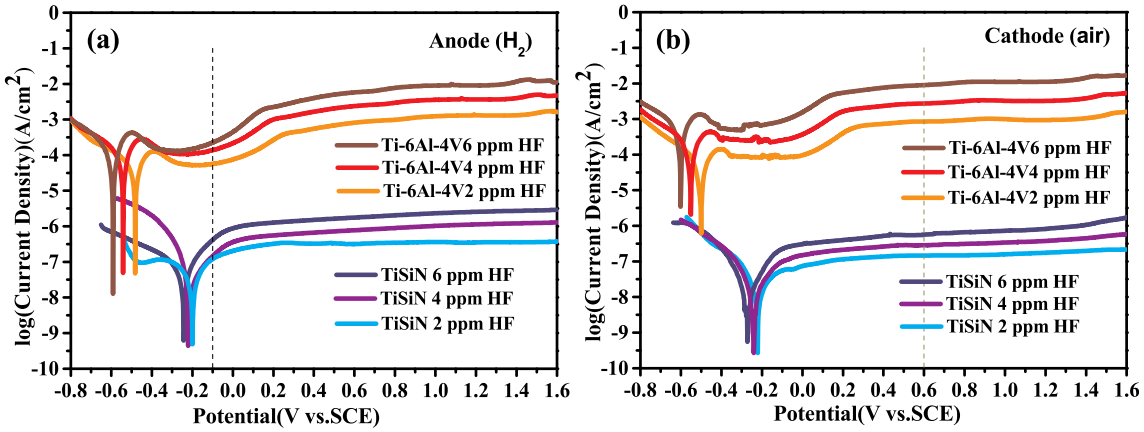

Fig. 8. The potentiodynamic polarization curves for the TiSiN coating and uncoated Ti-6A1-4 V in simulated anodic (purged with H_2) (a) and cathodic (purged with air) (b) condition in 0.5 M H_2SO_4 solution with different concentrations of HF (namely, 2,4 and 6 ppm) at 70 °C.

Table 2
Electrochemical parameters for the TiSiN coating and uncoated Ti–6Al–4V obtained from polarization curves.

Samples	E_{corr}	i_{corr}	β_a	-βc	$i_{0.6V}$ or $i_{-0.1V}$	P_e
	(V vs. SCE)	(A cm^{-2})	(mV/decade)	(mV/decade)	(A· cm^{-2})	
Cathode						
Ti–6Al–4V 2 ppm	−0.5	1.24×10^{-5}	247.15	189.64	8.51×10^{-4}	–
Ti–6Al–4V 4 ppm	−0.55	4.45×10^{-5}	223.45	200.45	2.75×10^{-3}	–
Ti–6Al–4V 6 ppm	−0.61	6.83×10^{-5}	212.34	212.35	6.19×10^{-3}	–
TiSiN 2 ppm	−0.22	7.14×10^{-8}	265.62	118.94	1.46×10^{-7}	99.98%
TiSiN 4 ppm	−0.24	8.32×10^{-8}	258.39	119.76	2.54×10^{-7}	99.99%
TiSiN 6 ppm	−0.27	9.78×10^{-8}	234.53	123.17	5.68×10^{-7}	99.99%
Anode						
Ti–6Al–4V 2 ppm	−0.48	8.03×10^{-6}	258.53	201.36	5.75×10^{-5}	–
Ti–6Al–4V 4 ppm	−0.54	1.02×10^{-5}	235.42	214.53	1.13×10^{-4}	–
Ti–6Al–4V 6 ppm	−0.59	1.16×10^{-5}	221.13	234.43	1.91×10^{-4}	–
TiSiN 2 ppm	−0.2	2.35×10^{-8}	271.15	118.45	1.21×10^{-7}	99.79%
TiSiN 4 ppm	−0.22	3.47×10^{-8}	265.12	121.34	1.85×10^{-7}	99.84%
TiSiN 6 ppm	−0.24	4.13×10^{-8}	242.17	122.21	2.74×10^{-7}	99.86%

HF concentration of 2 ppm, the intersection of the uncoated substrate shifts from A to C with a ΔE_{corr} of ~0.24 V and Δi_{corr} of ~ -1.5×10^{-5} A/cm^2, and the intersection of the TiSiN coating shifts from D to F with a ΔE_{corr} of ~0.12 V and Δi_{corr} of ~ -2.3×10^{-7} A/cm^2. The larger values of $|\Delta E_{corr}|$ and $|\Delta i_{corr}|$ for the uncoated substrate indicate that the uncoated alloy depends more on protection from the passive film compared with the TiSiN coating. That is, the corrosion rate of the uncoated Ti–6Al–4V is more sensitive to deterioration of the passive layer. As the HF concentration increases from 2 ppm to 6 ppm, the intersection of the uncoated alloy shifts from C to B with a ΔE_{corr} of -0.11 V and Δi_{corr} of -1.2×10^{-5} A/cm^2, and the intersection of the TiSiN coating shifts from F to E with a ΔE_{corr} of -0.05 V and Δi_{corr} of $\sim 5.8 \times 10^{-8}$ A/cm^2. The larger values of $|\Delta E_{corr}|$ and $|\Delta i_{corr}|$ for the uncoated substrate indicate that the passive layers formed on the uncoated alloy deteriorate more severely than that on the TiSiN coating with increasing HF concentration. Therefore, the TiSiN coatings exhibit higher chemical inertness against the aggressive attack from HF than the uncoated substrate in simulated PEMFC environments.

3.3.3. Potentiostatic polarization measurements and XPS analysis

In order to investigate the corrosion behavior of the TiSiN coating and the uncoated alloy under the harsh working conditions of a PEMFC, the current density as a function of time was obtained in simulated anodic (at -0.1 V_{SCE} shown in Fig. 10 (a)) and cathodic (at 0.6 V_{SCE} shown in Fig. 10 (b)) PEMFC environments with different HF concentrations. The current densities of the TiSiN coating and the uncoated substrate at the steady-state are summarized in Table 3. With increasing HF concentration, a higher current density can be observed for both the uncoated Ti–6Al–4V and the TiSiN coating. This shows that the HF can accelerate the corrosion process in both cases. For a given HF concentration, the current density of the uncoated Ti–6Al–4V is about three orders of magnitude greater than that of the TiSiN coating under a simulated anodic environment, and this difference in the current density is larger at the simulated cathodic environment due to the transpassivation of the uncoated substrate. As such, the TiSiN coating exhibits much higher corrosion resistance than the substrate under simulated PEMFCs operational environments. Finally, the values of the current density of the TiSiN coating stabilized at approximately 10^{-7} A cm^{-2}, and so readily meet the U.S. Department of Energy (DoE) 2020 target of 1 μA cm^{-2} for the corrosion rate under PEMFC operating conditions [63].

In addition, the current density of the TiSiN coating decreases significantly at the initial stage of corrosion and then stabilizes within 200 s. However, more time is required to reach the steady state for the uncoated alloy. Furthermore, the current density curves of the TiSiN coating are smooth and nearly constant compared to the uncoated substrate. This shows that the TiSiN coating inhibits corrosion reactions more rapidly and steadily than the passive layers present on the uncoated alloy under the simulated working conditions of a PEMFC.

To elucidate the chemical state of the surface of the TiSiN coating

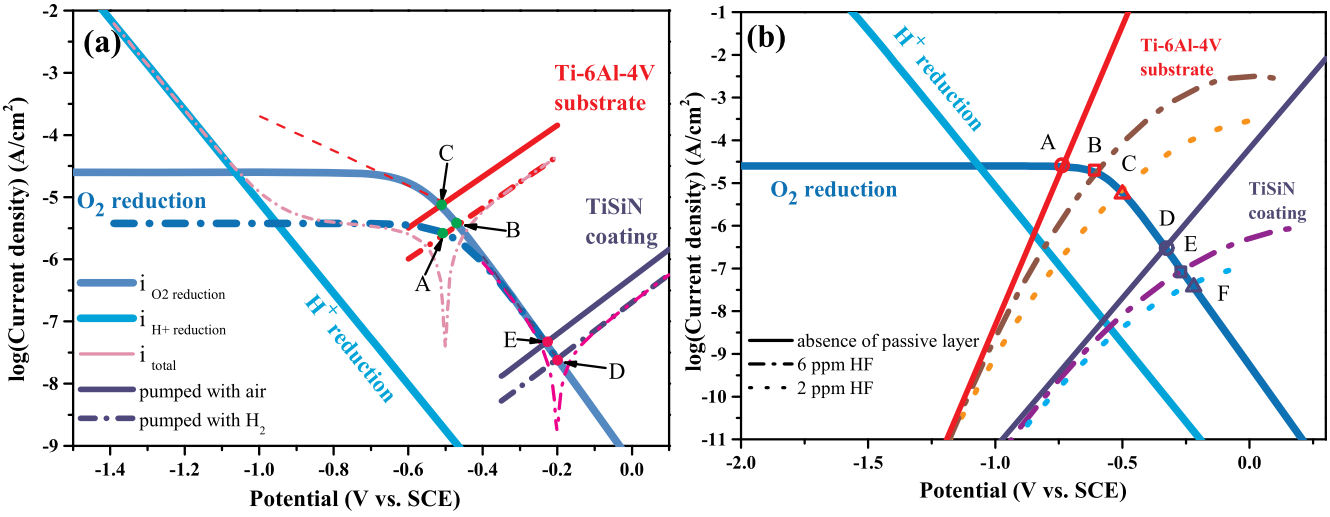

Fig. 9. Evans' diagram illustration for the corrosion behavior of the TiSiN coating and the uncoated Ti-6A1-4 V at the given HF concentration of 2 ppm (a) and under the cathode condition (b).

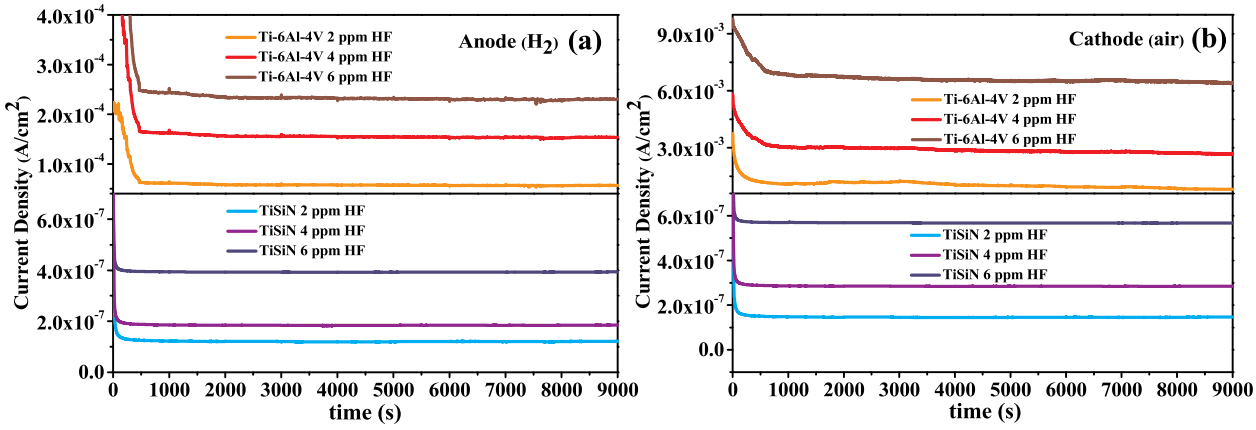

Fig. 10. Potentiostatic polarization curves of the TiSiN coating and the uncoated Ti-6A1-4 V at cathode (+0.6 V_{SCE} purged with air) (a) and anode (−0.1 V_{SCE} purged with H_2) (b) potentials in 0.5 M H_2SO_4 solution with different concentrations of HF (namely, 2,4 and 6 ppm) at 70 °C.

Table 3
Electrochemical parameters for the TiSiN coating and uncoated Ti–6Al–4V obtained from potentiostatic polarization.

Samples	Cathode Current Density	Anode Current Density
Ti–6Al–4V 2 ppm	1.17×10^{-4} A cm^{-2}	5.91×10^{-5} A cm^{-2}
Ti–6Al–4V 4 ppm	2.92×10^{-3} A cm^{-2}	1.46×10^{-4} A cm^{-2}
Ti–6Al–4V 6 ppm	6.73×10^{-3} A cm^{-2}	2.39×10^{-4} A cm^{-2}
TiSiN 2 ppm	1.62×10^{-7} A cm^{-2}	1.31×10^{-7} A cm^{-2}
TiSiN 4 ppm	2.84×10^{-7} A cm^{-2}	1.94×10^{-7} A cm^{-2}
TiSiN 6 ppm	5.88×10^{-7} A cm^{-2}	3.93×10^{-7} A cm^{-2}

after corrosion, XPS was performed on sample subjected to the potentiostatic polarization test under the cathodic condition with a HF concentration of 6 ppm. XPS survey spectra and the high-resolution XPS spectra for Ti 2p, Si 2p and N1s are shown in Fig. 11 (a)-(d). From the XPS full spectrum of the coating (shown in Fig. 11 (a)), an additional intense peak from O1s is observed on the corroded specimen compared with the XPS analysis of the specimen before corrosion. This indicates that an oxide passive layer formed on the TiSiN coating.

Fig. 11 (b) shows the doublet Ti 2p3/2 and Ti 2p1/2 peaks, exhibiting evident asymmetry, can be fitted to six Gaussian functions. The doublet peaks located at 454.83 eV and 460.63 eV were assigned to Ti–N bonds in TiN. The strong signal from TiSiN coating in the XPS spectra shows that the oxide layer on the TiSiN coating is thin. The doublet peaks, with the highest binding energies at 457.88 eV and 463.68 eV, corresponded to Ti–O bonds in TiO_2 [64]. Between these two sets of peaks, the other doublet peaks, with binding energies of 455.72 eV and 461.52 eV, are regarded as an intermediate phase between TiN and TiO_2 ascribed, by others, to the suboxides of titanium [64–66]. According to the N 1s spectrum, these doublet peaks are suggested to originate from titanium oxynitrides (TiO_xN_y) in this study, which explains the presence of the shoulder peak with a binding energy of 396.48 eV, lower than that of the N–Ti bonds in the N 1s spectrum (shown in Fig. 11 (c)) [65,66]. From quantitative evaluations of the Ti

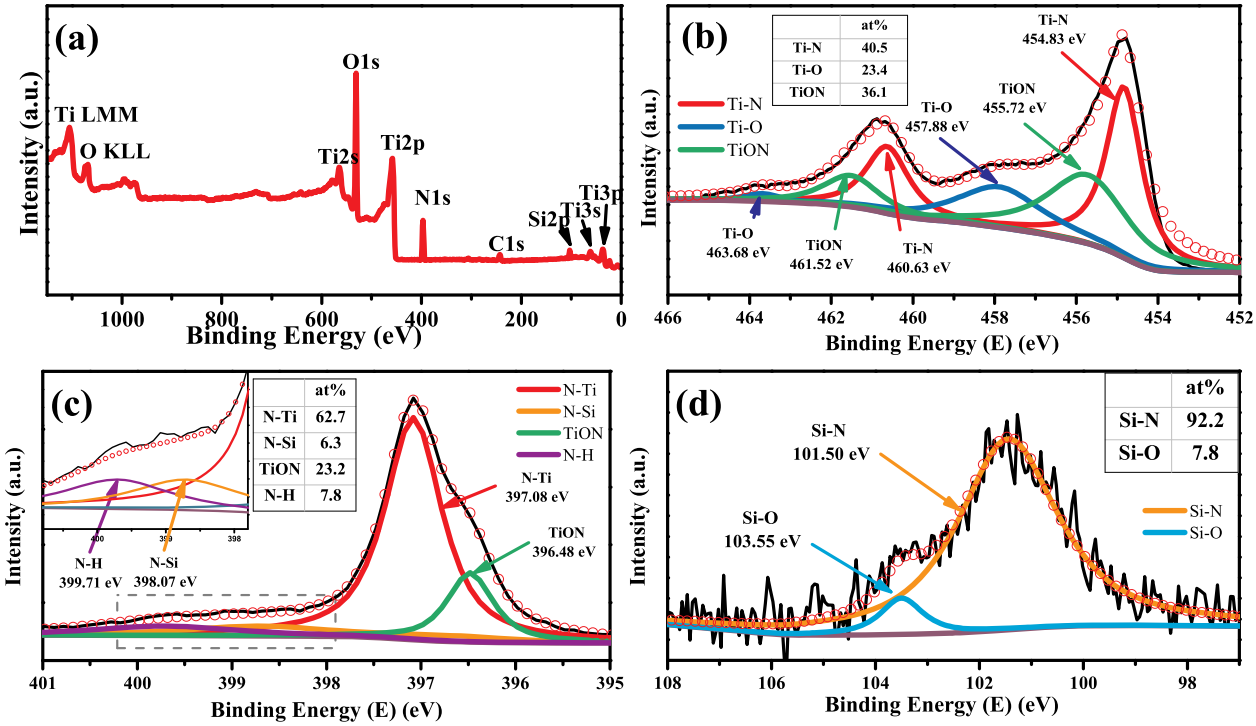

Fig. 11. (a) XPS survey spectra and the high-resolution XPS spectra for Ti 2p (b), Si 2p (c) and N1s (d) peaks collected from the TiSiN coated sample after the potentiostatic polarization test at +0.6 V_{SCE} purged with air for 2.5 h in a 0.5 M H_2SO_4 + 6 ppm HF solution.

2p spectrum, the phase fraction of TiO_xN_y is higher than that of TiO_2 suggesting that the oxide passive layer present on the TiSiN coating is highly doped by nitrogen atoms.

The N1s core level spectrum can be deconvoluted into four Gaussian peaks shown in Fig. 11 (c). The peaks with binding energies of 396.48 eV, 397.08 eV and 398.71 eV arise from TiO_xN_y, TiN and Si_3N_4, respectively. The peak located at 399.71 eV is considered to be the characteristic of NH_4^+ corresponding to nitride corrosion products [67,68]. The formation of NH_4^+ neutralizes H^+ and partially buffers the acidity on the surface of the TiSiN coating during the potentiostatic polarization test [69].

As shown in Fig. 11 (d), the Si 2p spectrum can be deconvoluted into a strong peak at 101.50 eV and a weaker shoulder peak at 103.55 eV corresponding to the Si–N bonds in Si_3N_4 and Si–O bonds in SiO_2, respectively [70]. From quantitative evaluations of the Si 2p peak, the phase fraction of SiO_2 is much lower than that of Si_3N_4 in the oxide passive layer due to etching by HF (i.e. $SiO_2 + 4H^+ + 6F^- = 2H_2O + SiF_6^{2-}$) [71]. Nevertheless, the reaction between SiO_2 and F^- ions can inhibit the permeation of F^- ions into the coating. Meanwhile, the SiF_6^{2-} ion, as a chemically stable product of this reaction, undergoes competitive adsorption with F^- ions on the surface of the passivation layer. Thus, with the addition of Si, the TiSiN coating is slightly influenced by the HF concentration compared with the uncoated substrate.

To simply compare the corrosion resistance of the TiSiN coating and the uncoated alloy, typical surface morphologies of both samples before, and after, 2.5 h potentiostatic polarization in the simulated cathodic condition with addition of 6 ppm HF were examined using a SEM. As shown in Fig. 12, the surface of the uncoated Ti–6Al–4V sample is severely corroded with evidence of active dissolution and pitting corrosion clearly observed. However, almost no pits, pinholes or micropores were observed on the surface of the TiSiN coating. Thus, the enhancement in protection afforded by a TiSiN coating to bipolar plates in a simulated PEMFC environment is evident.

3.3.4. Electrochemical impedance measurements

Typical Bode and Nyquist plots for the TiSiN coating and bare titanium alloy at their respective E_{OCP} in 0.5 M H_2SO4 solution containing different HF concentrations (i.e. 2 ppm, 4 ppm and 6 ppm) at 70 °C after potentiostatic polarization testing under cathodic conditions are shown in Fig. 13 (a)-(d). For any given HF concentration, the Nyquist plots for both samples display an incomplete capacitive semicircle over the complete frequency range. The diameter of the capacitive arc for the TiSiN coating is larger than that for the uncoated substrate. From the Bode plots, the TiSiN coating shows a broad plateau with the phase angle maxima near −90° corresponding to the linear variation between log |Z| and log f (frequency) with a slope of almost −1 at the low and middle frequency range. By comparison, the titanium alloy substrate exhibits a single monosymmetric narrow peak with phase angle increase up to a maximum of −75°. The linear region is not maintained at low frequencies (below 0.1 Hz) with a decrease of phase angle. These plots suggest that the passive films on the TiSiN coating exhibit a purer capacitive behavior [72] when immersed in an aggressive medium compared to that on the uncoated substrate [73]. With increasing HF concentration, more depressed capacitive semicircles are observed in the Nyquist plots for both samples. Meanwhile, the maximum phase angle deceases together with a narrower linear region and low-frequency limit |Z| as shown in the Bode plots, suggesting that the corrosion resistance of both samples is reduced by HF.

To extract detailed information about the kinetics of the complex electrochemical processes, the appropriate equivalent electrical circuits (EECs) were chosen to model and interpret the EIS data. For the uncoated Ti–6Al–4V, an equivalent electrical circuit $R_s(Q_pR_p)$ (given in Fig. 14 (a)) is adopted due to the one time constant process presented in the Bode phase plots over a range of frequencies from 10^{-2} – 10^5 Hz. In this corrosion system, R_s and R_p represents the resistance of the solution and the passive film, respectively, and Q_p is a constant phase element (CPE) related to the capacitance behaviour of the passive film. In the case of TiSiN coating, the asymmetric broad peak in the Bode phase plots appears to derive from two time constant process corresponding to the electrochemical behaviour in the medium frequency and low frequency regions, respectively. Thus, the equivalent electrical circuit $R_s(Q_{dl}R_{ct}(Q_cR_c))$ (shown in Fig. 14 (b)) was adopted, where R_{ct} and Q_{dl} in the primary circuit represent, respectively, the charge transfer resistance and double layer capacitance from the interface of the solution/coating, R_c and Q_c in the secondary circuit represent, respectively,

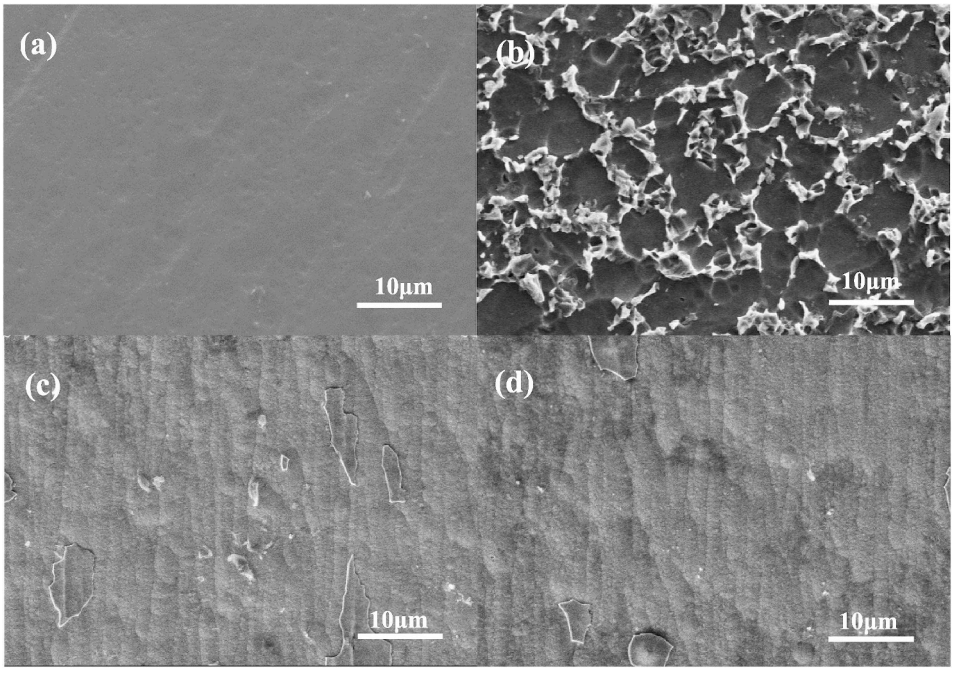

Fig. 12. Secondary electron images of the corroded surface morphologies of (a, b) uncoated Ti-6A1-4 V and (c, d) the TiSiN coating before (a, c) and after (b, d) potentiostatic testing in the simulated cathodic condition with 0.5 M H_2SO_4 + 6 ppm HF solution for 2.5 h.

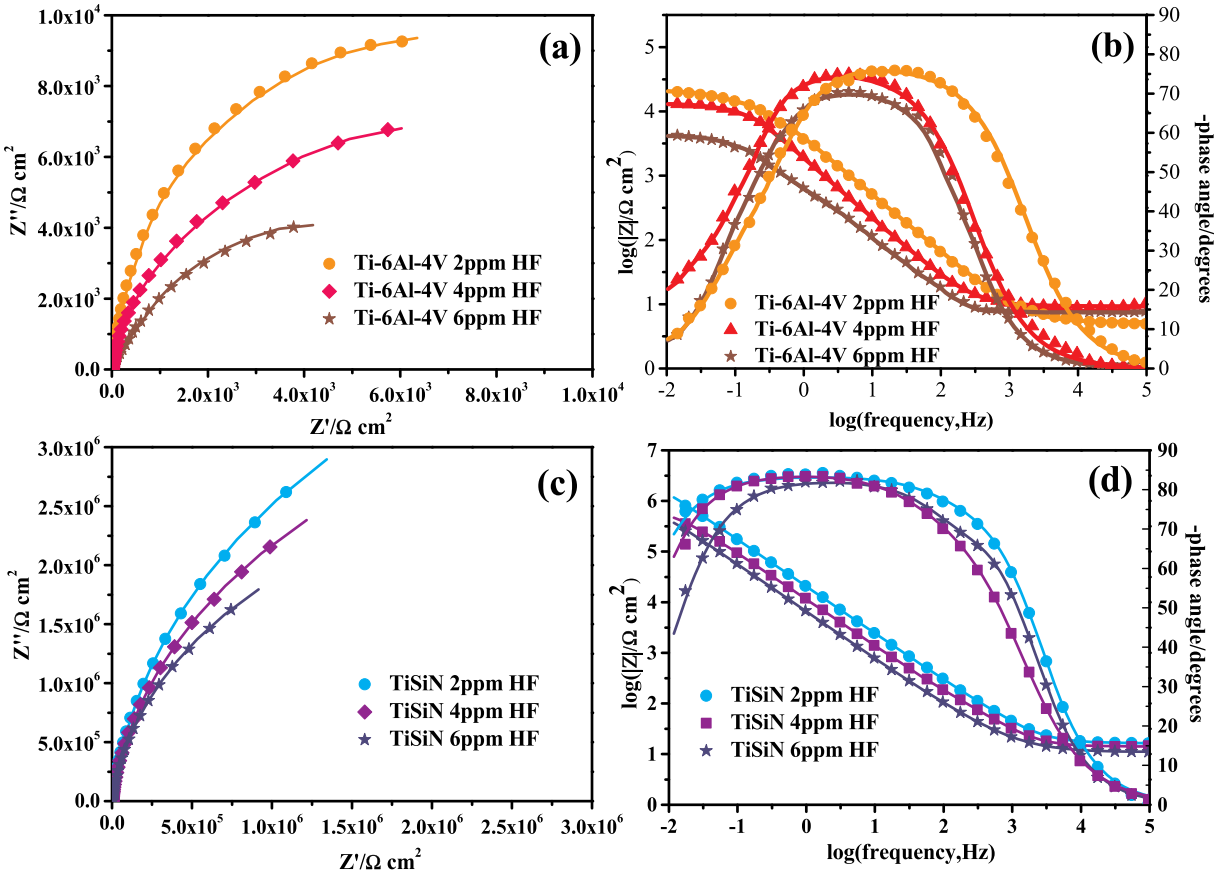

Fig. 13. Representative Nyquist and Bode plots for uncoated and the TiSiN coated Ti–6Al–4V at their respective E_{OCP} in 0.5 M H_2SO_4 solution containing different HF concentrations at 70 °C. The bare Ti–6Al–4V: (a) Nyquist plot, (b) Bode plot; the TiSiN coating: (c) Nyquist plot, (d) Bode plot.

the resistance and pseudo-capacitance of the coating. However, the parameters of the elements based on this EEC are not reliable due to a larger value of χ^2 (with the order of magnitude greater than 10^{-2}). In particular, the relative standard error of the parameters for R_{ct} and Q_{dl} are over 100%, indicating that Q_{dl} and R_{ct} in the secondary circuit are inappropriate for the electrochemical response arising from the interface of solution/coating. This large fitting error may be related to the following reasons. First, due to the similar dielectric properties between the TiSiN coating and the passive film, the capacitive response of the passive film is difficult to distinguish from that of the TiSiN coating, which leads to a single time constant [74]. Second, a larger number of F^- ions and oxygen are located on the surface of the TiSiN coating during the polarization process. This can lead to a diffusion controlling step [75]. Therefore, in order to better fit the EIS data of the TiSiN coating, the equivalent electrical circuit $R_s(Q_p(R_pO))$ was employed as shown in Fig. 14 (c). The elements R_p and Q_p represent resistance and the capacitance, respectively, contributed by the passive layer and the TiSiN coating. The cotangent–hyperbolic diffusion impedance (O) can be used to simulate the finite length diffusion process on the surface of the TiSiN coating. The fitting parameters are summarized in Table 4.

At a given HF concentration, R_p for the TiSiN coating is three or four orders of magnitude greater than that for the uncoated substrate, indicating that the resistance to charge transfer and point defect migration is much higher for the TiSiN coating than that for the uncoated alloy. The TiSiN coating retards the oxidizing reaction and the dissolution of metal ions and provides good protection for the substrate. In addition, the constant phase element and the factor n are used to describe a leaky capacitor deviating from that of an ideal capacitor. When n is equal to 1 the CPE represents an ideal capacitor. Where n is less than 1, the CPE describes a frequency dispersion of time constants because of heterogeneities such as roughness, porosity and other inhomogeneities which may be present [76]. The value of n for the TiSiN coating is larger than that for the uncoated alloy, denoting that the passive film on the TiSiN coating offers a better barrier property against corrosive attack than that on bare substrate. As the HF concentration increases, the values of R_p and n for the uncoated Ti–6Al–4V decrease more sharply than that for the TiSiN coating, suggesting that the TiSiN coating provides protection for the substrate in solutions that contain HF. Furthermore, the capacitance of O is slightly influenced by the HF concentration, indicating that TiSiN can effectively impede the diffusion of F^- ions and oxygen. Small variations in the diffusion of F^- ions and oxygen may arise from the microstructure of the TiSiN coating.

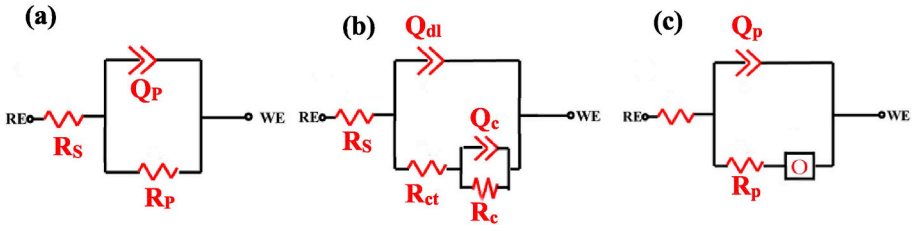

Fig. 14. Equivalent electrical circuits used for modeling experimental EIS data, (a) $R_s(Q_pR_p)$, (b) $R_s(Q_{dl}R_{ct}(Q_cR_c))$, (c) $R_s(Q_p(R_pO))$.

Table 4
Electrochemical parameters obtained from equivalent circuits simulation.

		R_s (Ω cm^2)	Q_P (Ω^{-1} cm^{-2} s^n)	R_P (Ω cm^2)	n	O (Ω^{-1} cm^{-2} $\sqrt{s}$)	χ^2
Ti–6Al–4V	2 ppm HF	10.43 ± 0.01	(3.47 ± 0.01) × 10^{-5}	(5.52 ± 0.04) × 10^4	0.82	–	3.47 × 10^{-3}
	4 ppm HF	11.56 ± 0.02	(5.62 ± 0.01) × 10^{-5}	(2.41 ± 0.03) × 10^4	0.78	–	5.21 × 10^{-3}
	6 ppm HF	11.32 ± 0.01	(6.67 ± 0.02) × 10^{-5}	(9.03 ± 0.02) × 10^3	0.72	–	4.42 × 10^{-3}
TiSiN coating	2 ppm HF	14.36 ± 0.01	(1.13 ± 0.01) × 10^{-7}	(7.56 ± 0.02) × 10^7	0.92	(4.11 ± 0.01) × 10^{-7}	5.26 × 10^{-4}
	4 ppm HF	14.28 ± 0.02	(4.42 ± 0.02) × 10^{-7}	(4.20 ± 0.01) × 10^7	0.91	(3.89 ± 0.02) × 10^{-7}	3.14 × 10^{-4}
	6 ppm HF	13.31 ± 0.01	(5.17 ± 0.03) × 10^{-7}	(2.36 ± 0.02) × 10^7	0.91	(4.06 ± 0.02) × 10^{-7}	5.34 × 10^{-3}

Silicon additions to TiN coatings promote the formation of equiaxed grains rather than the columnar structures usually seen in PVD prepared coatings (as shown in Fig. 4). The zig-zag grain boundaries of the equiaxed structure significantly increases the diffusion path for both F^- ions and oxygen and so a sharp reduction in the concentration of F^- ions and oxygen at the interface between the solution and the TiSiN coating [77].

3.4. Interfacial contact resistance

Interfacial contact resistance (ICR) arises from the interface that exists between the gas diffusion layer (GDL) and the bipolar plate. This parameter is critical in evaluating the conductivity and the power output loss of a PEMFC stack [78]. The values for the ICR for both coated and uncoated specimens, as a function of compaction force, both before, and after, the potentiostatic polarization test are presented in Fig. 15. Under an applied compaction force of 140 N cm^{-2} (which is applied in conventional fuel cell stacks) before the potentiostatic polarization test, the ICR values of the uncoated alloy and the TiSiN coating were 98.9 mΩ cm^{-2} and 14.7 mΩ cm^{-2}, respectively. After the potentiostatic polarization test, the values for ICR for the uncoated alloy and TiSiN coating increased to 128.2 mΩ cm^{-2} and 18.3 mΩ cm^{-2}, respectively. It is evident that the ICR of the TiSiN coating is much less than the uncoated substrate in a simulated PEFMC environment. This means that the TiSiN coated bipolar plates exhibit better conductivity in the PEMFC and thus reduce the power loss of the PEMFC compared to titanium alloy bipolar plates.

Values of ICR are significantly affected by the surface state of the bipolar plate, e.g. the composition and roughness at the material surfaces [79]. For the uncoated titanium alloy, a TiO_2 oxide layer spontaneously forms on the sample surface. Due to the low electrical conductivity of TiO_2, the uncoated Ti–6Al–4V always exhibits a high ICR value. Following corrosion, leading to thickening of the oxide layer and roughening of the outer surface, the resistance of the oxide layer increased and the effective contact area between GDL and bipolar plate decreased resulting in a further increase of the ICR for the uncoated alloy [80]. However, the TiSiN coating exhibits lower ICR due to the good electrical conductivity of the TiN phase arising from the nine valence electrons associated with the strongly hybridized Ti 3d and N 2p orbitals [81,82]. After corrosion, a thin and nitrogen-rich-doping oxide layer formed on the TiSiN coating, the presence of which was confirmed by XPS analysis. TiO_xN_y has been shown to exhibit high metallic conductivity where the electrical conductivity increases with increasing nitrogen content [83]. As such, the ICR is not strongly influenced by the oxide layer formed on the TiSiN coating. Furthermore, no visible change in surface roughness was observed on the TiSiN coating, so it retains its effective contact area. Thus, the TiSiN coating maintains a low ICR in the simulated PEFMC environment compared to the uncoated Ti–6Al–4V.

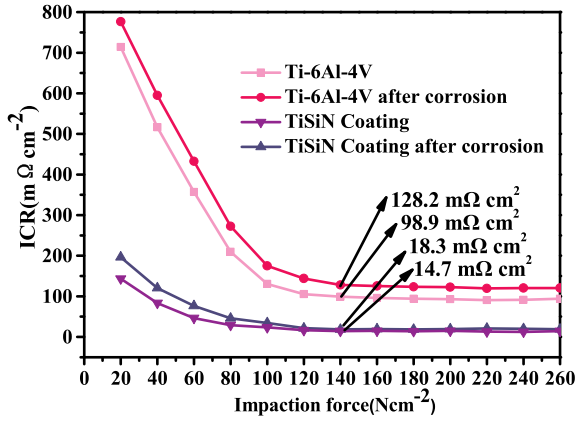

Fig. 15. The interfacial contact resistance (ICR) as a function of compaction force from 20 to 260 N cm^{-2} for the TiSiN coating and uncoated Ti-6A1-4 V before and after 2.5 h potentiostatic polarization at a cathode potential of + 0.6 V_{SCE} in 0.5 M H_2SO_4 + 6 ppm HF solution open to air at 70 °C.

3.5. Contact angle measurements

Water, as a waste product in PEMFC stacks, can prevent the dehydration of the proton exchange membrane. However, redundant liquid water blocks access of reaction gases to the electrodes and also increases the rate of corrosion of the bipolar plates. As such, it needs to be removed in a timely way [84]. Therefore, the bipolar plates that exhibit good hydrophobicity are beneficial for the water management in the PEMFC. To determine the hydrophobicity of the TiSiN coating and the uncoated alloy, the water contact angles were measured from photographs of water droplets on the surface of the samples as shown in Fig. 16. The water contact angles for the uncoated substrate and the TiSiN coating are 61.2°and 93.4°, respectively. Clearly, the TiSiN coating increases the water contact angle relative to the titanium alloy substrate. In general, water is a polar liquid and is likely to be adsorbed on the surface due to its higher polar contributions [85]. Metal nitrides are reported to increase the hydrophobicity of original surface for the substrate due to their non-polar nature of their surface chemistry compared to the substrate [80,86]. Thus, the TiSiN coating gives improved hydrophobicity to the Ti alloy bipolar plates.

4. Conclusion

A dense, uniform TiSiN coating was deposited onto a Ti–6Al–4V substrate by reactive-sputter-deposition. The TiSiN coating consisted of TiN grains 5–10 nm in diameter with a Si_3N_4 amorphous phase located at the grain boundaries. The electrochemical behavior of both the TiSiN coating and uncoated titanium substrate were investigated in a simulated PEMFC environment with different concentrations of HF. For a given HF concentration, the TiSiN coating exhibited a higher corrosion potential and a lower corrosion current density. This suggests a reduced tendency for corrosion and a lower rate of corrosion rate compared with the uncoated alloy. The passive film presented on the TiSiN coating showed excellent chemical inertness with the significantly higher R_p than that on the uncoated alloy, which thus provides good corrosion resistance. With increases in HF concentration, the corrosion rate was accelerated for both specimens. Deterioration of the corrosion resistance for the TiSiN coatings is much less than the uncoated substrate due to the coating acting as an effective barrier to the permeation of F^-

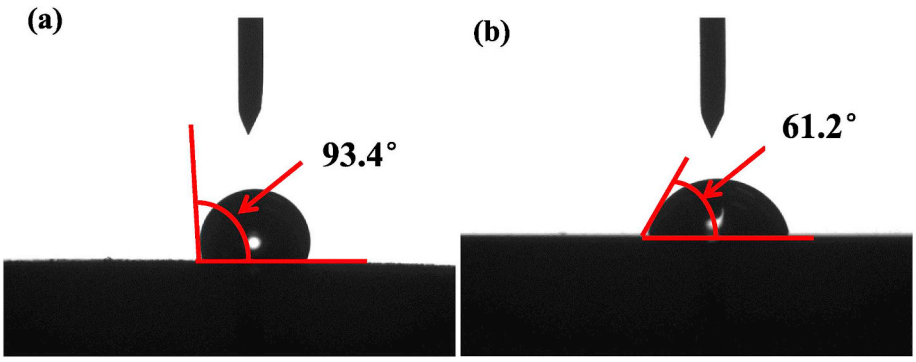

Fig. 16. Photographs of water droplet on the TiSiN coating (a) and the bare Ti–6Al–4V alloy (b).

ions and oxygen. Therefore, the TiSiN coatings provides excellent protection for the titanium alloy substrate against the corrosion from a typical PEMFC operating environment. Furthermore, the TiSiN coating exhibits lower ICR than titanium alloy substrate both before and after corrosion testing, which helps reduce the power loss of the PEMFC. The high hydrophobicity of the TiSiN coating also facilitates effective liquid water removal from the bipolar plates. To sum up, the deposited coating exhibited a combination of good corrosion resistance, hydrophobicity and a low ICR that offers potential for enhancing the durability and performance of metallic bipolar plates used in PEMFCs.

Declaration of competing interest

The authors declare that they have no known competing financial interests or personal relationships that could have appeared to influence the work reported in this paper.

Acknowledgement

The authors acknowledge research funding from the General Program of the National Natural Science Foundation of China (grant no. 51675267) and the Key Program of the National Natural Science Foundation of China (grant no. 51635004). Australian Research Council support through the Discovery Projects program (grant no. DP150102417) is also acknowledged.

References

[1] Y. Wang, D.O. Northwood, An investigation into TiN-coated 316L stainless steel as a bipolar plate material for PEM fuel cells, J. Power Sources 165 (2007) 293–298.
[2] V. Mehta, J.S. Cooper, Review and analysis of PEM fuel cell design and manufacturing, J. Power Sources 114 (2003) 32–53.
[3] H.C. Chen, Z. Song, X. Zhao, T. Zhang, P.C. Pei, C. Liang, A review of durability test protocols of the proton exchange membrane fuel cells for vehicle, Appl. Energy 224 (2018) 289–299.
[4] Q. Hu, D. Zhang, H. Fu, K. Huang, Investigation of stamping process of metallic bipolar plates in PEM fuel cell-Numerical simulation and experiments, Int. J. Hydrogen Energy 39 (2014) 13770–13776.
[5] E. Middelman, W. Kout, B. Vogelaar, J. Lenssen, E. de Waal, Bipolar plates for PEM fuel cells, J. Power Sources 118 (2003) 44–46.
[6] J.S. Cooper, Design analysis of PEMFC bipolar plates considering stack manufacturing and environment impact, J. Power Sources 129 (2004) 152–169.
[7] Y.J. Ren, C.L. Zeng, Corrosion protection of 304 stainless steel bipolar plates using TiC films produced by high-energy micro-arc alloying process, J. Power Sources 171 (2007) 778–782.
[8] K. Feng, Z.G. Li, Effect of microstructure of TiN film on properties as bipolar plate coatings in polymer electrolyte membrane fuel cell prepared by inductively coupled plasma assisted magnetron sputtering, Thin Solid Films 544 (2013) 224–229.
[9] A. Hermann, T. Chaudhuri, P. Spagnol, Bipolar plates for PEM fuel cells: a review, Int. J. Hydrogen Energy 30 (2005) 1297–1302.
[10] R.J. Tian, J.C. Sun, Corrosion resistance and interfacial contact resistance of TiN coated 316L bipolar plates for proton exchange membrane fuel cell, Int. J. Hydrogen Energy 36 (2011) 6788–6794.
[11] H. Rashtchi, Y.A. Gomez, K. Raeissi, M. Shamanian, B. Eriksson, M. Zhiani, C. Lagergren, R.W. Lindstrom, Performance of a PEM fuel cell using electroplated Ni-Mo and Ni-Mo-P stainless steel bipolar plates, J. Electrochem. Soc. 164 (2017) F1427–F1436.
[12] N.F. Asri, T. Husaini, A. Sulong, E.H. Majlan, W.R.W. Daud, Coating of stainless steel and titanium bipolar plates for anticorrosion in PEMFC: a review, Int. J. Hydrogen Energy 42 (2017) 9135–9148.
[13] C.K. Jin, M.G. Jung, C.G. Kang, Fabrication of aluminum bipolar plates by semi-solid forging process and performance test of TiN coated aluminum bipolar plates, Fuel Cells 14 (2014) 551–560.
[14] J.Y. Lin, C.Y. Lin, S.K. Liu, C.C. Wan, Y.Y. Wang, Characterization of electroless Ni-based alloys for use in bipolar plates of direct methanol fuel cells, Surf. Coat. Technol. 205 (2010) 2251–2255.
[15] T. Ous, C. Arcoumanis, Degradation aspects of water formation and transport in proton exchange membrane fuel cell: a review, J. Power Sources 240 (2013) 558–582.
[16] H. Tawfik, Y. Hung, D. Mahajan, Metal bipolar plates for PEM fuel cell - a review, J. Power Sources 163 (2007) 755–767.
[17] K. Feng, Y. Shen, H. Sun, D. Liu, Q. An, X. Cai, P.K. Chu, Conductive amorphous carbon-coated 316L stainless steel as bipolar plates in polymer electrolyte membrane fuel cells, Int. J. Hydrogen Energy 34 (2009) 6771–6777.
[18] H. Wang, J.A. Turner, Reviewing metallic PEMFC bipolar plates, Fuel Cells 10 (2010) 510–519.
[19] M. Bin-Sudin, A. Leyland, A.S. James, A. Matthews, J. Housden, B. Garside, Substrate surface finish effects in duplex coatings of PAPVD TiN and CrN with electroless nickel-phosphorus interlayers, Surf. Coat. Technol. 81 (1996) 215–224.
[20] T. Polcar, T. Kubart, R. Novák, L. Kopecký, P. Široký, Comparison of tribological behaviour of TiN, TiCN and CrN at elevated temperatures, Surf. Coat. Technol. 193 (2005) 192–199.
[21] G.E. Weng, A.K. Ling, X.Q. Lv, J.Y. Zhang, B.P. Zhang, III-Nitride-Based quantum dots and their optoelectronic applications, Nano-Micro Lett. 3 (2011) 200–207.
[22] E.A. Cho, U.S. Jeon, S.A. Hong, I.H. Oh, S.G. Kang, Performance of a 1kW-class PEMFC stack using TiN-coated 316 stainless steel bipolar plates, J. Power Sources 142 (2005) 177–183.
[23] D.M. Zhang, L.T. Duan, L. Guo, Z.Y. Wang, J. Zhao, W.H. Tuan, K. Niihara, TiN-coated titanium as the bipolar plate for PEMFC by multi-arc ion plating, Int. J. Hydrogen Energy 36 (2011) 9155–9161.
[24] D. Biro, M.P. Hasaneen, L. Szekely, M. Menyhard, S. Gurban, P. Pekker, I. Dodony, P.B. Barna, Texture change of TiN films due to anisotropic incorporation of oxygen, Vacuum 103 (2014) 78–86.
[25] L. Chen, Y. Du, S.Q. Wang, A.J. Wang, H.H. Xu, Mechanical properties and microstructural evolution of TiN coatings alloyed with Al and Si, Mater. Sci. Eng. A-Struct. 502 (2009) 139–143.
[26] D.E. Wolfe, B.M. Gabriel, M.W. Reedy, Nanolayer (Ti,Cr)N coatings for hard particle erosion resistance, Surf. Coat. Technol. 205 (2011) 4569–4576.
[27] Y.H. Yoo, D.P. Le, J.G. Kim, S.K. Kim, P. Van Vinh, Corrosion behavior of TiN, TiAlN, TiAlSiN thin films deposited on tool steel in the 3.5 wt.% NaCl solution, Thin Solid Films 516 (2008) 3544–3548.
[28] M.T. Lin, C.H. Wan, W.T. Wu, Comparison of corrosion behaviors between SS304 and Ti substrate coated with (Ti,Zr)N thin films as Metal bipolar plate for unitized regenerative fuel cell, Thin Solid Films 544 (2013) 162–169.
[29] S.Y. Kim, D.H. Han, J.N. Kim, J.J. Lee, Titanium oxynitride films for a bipolar plate of polymer electrolyte membrane fuel cell prepared by inductively coupled plasma assisted reactive sputtering, J. Power Sources 193 (2009) 570–574.
[30] J. Xu, G.D. Wang, X. Lu, L. Liu, P. Munroe, Z.-H. Xie, Mechanical and corrosion-resistant properties of Ti-Nb-Si-N nanocomposite films prepared by a double glow discharge plasma technique, Ceram. Int. 40 (2014) 8621–8630.
[31] J. Xu, Z. Li, S. Xu, P. Munroe, Z.-H. Xie, A nanocrystalline zirconium carbide coating as a functional corrosion-resistant barrier for polymer electrolyte membrane fuel cell application, J. Power Sources 297 (2015) 359–369.
[32] J. Xu, J. Cheng, S. Jiang, P. Munroe, Z.-H. Xie, The influence of Ti additions on the mechanical and electrochemical behavior of β-Ta_5Si_3 nanocrystalline coating, Appl. Surf. Sci. 419 (2017) 901–915.
[33] W. Oliver, G.M.J. Pharr, An improved technique for determining hardness and elastic modulus using load and displacement sensing indentation experiments, J. Mater. Res. 7 (1992) 1564–1583.
[34] H. Wang, J.A. Turner, Ferritic stainless steels as bipolar plate material for polymer electrolyte membrane fuel cells, J. Power Sources 128 (2004) 193–200.
[35] J.L. He, C.K. Chen, M.H. Hon, Microstructure and properties of TiSiN films prepared by plasma-enhanced chemical vapor deposition, Mater. Chem. Phys. 44 (1996)

9–16.
[36] C.Y. Su, C.T. Lu, W.T. Hsiao, W.H. Liu, F.S. Shieu, Evaluation of the microstructural and photocatalytic properties of aluminum-doped zinc oxide coatings deposited by plasma spraying, Thin Solid Films 544 (2013) 170–174.
[37] S. Li, J. Deng, X. Qin, C. Ji, Effects of Ti target current on properties of TiSiN coatings, Surf. Eng. 33 (2017) 578–584.
[38] J. Pelleg, L.Z. Zevin, S. Lungo, N. Croitoru, Reactive-sputter-deposited TiN films on glass substrates, Thin Solid Films 197 (1991) 117–128.
[39] C. Feng, S. Zhu, M. Li, L. Xin, F. Wang, Effects of incorporation of Si or Hf on the microstructure and mechanical properties of Ti–Al–N films prepared by arc ion plating (AIP), Surf. Coat. Technol. 202 (2008) 3257–3262.
[40] A. Miletic, P. Panjan, B. Skoric, M. Cekada, G. Drazic, J. Kovac, Microstructure and mechanical properties of nanostructured Ti-Al-Si-N coatings deposited by magnetron sputtering, Surf. Coat. Technol. 241 (2014) 105–111.
[41] H.C. Barshilia, B. Deepthi, K.S. Rajam, Deposition and characterization of TiAlN/Si_3N_4 superhard nanocomposite coatings prepared by reactive direct current unbalanced magnetron sputtering, Vacuum 81 (2006) 479–488.
[42] J.C. Oliveira, F. Fernandes, F. Ferreira, A. Cavaleiro, Tailoring the nanostructure of Ti-Si-N thin films by HiPIMS in deep oscillation magnetron sputtering (DOMS) mode, Surf. Coat. Technol. 264 (2015) 140–149.
[43] M.S. Selamat, L.M. Watson, T.N. Baker, XRD and XPS studies of surface MMC layers developed by laser alloying Ti–6Al–4V using a combination of a dilute nitrogen environment and SiC powder, Surf. Coat. Technol. 201 (2006) 724–736.
[44] K. He, N.F. Chen, C.J. Wang, L.S. Wei, J.K. Chen, Method for determining crystal grain size by X-ray diffraction, Cryst. Res. Technol. 53 (2018) 6.
[45] W. Li, P. Liu, X. Zhu, K. Zhang, F. Ma, X. Liu, X. Chen, D. He, Influence of TiN-nanolayered insertions on microstructure and mechanical properties of TiSiN nanocomposite film, J. Mater. Sci. 49 (2014) 4127–4132.
[46] S. Guha, A. Bandyopadhyay, S. Das, B.P. Swain, Synthesis and characterization of titanium silicon nitride (TiSiN) thin film: a review, Mater. Sci. Eng. 377 (2018) 012181.
[47] F. Mei, N. Shao, X. Hu, G. Li, M. Gu, Microstructure and mechanical properties of reactively sputtered Ti-Si-N nanocomposite films, Mater. Lett. 59 (2005) 2442–2445.
[48] F. Kauffmann, B. Ji, G. Dehm, H. Gao, E. Arzt, A quantitative study of the hardness of a superhard nanocrystalline titanium nitride/silicon nitride coating, Scr. Mater. 52 (2005) 1269–1274.
[49] M.D. Bao, X.D. Zhu, J.W. He, Evaluation of toughness of hard coatings, Surf. Eng. 22 (2006) 11–14.
[50] M.F. Othman, A.R. Bushroa, W.N.R. Abdullah, Evaluation techniques and improvements of adhesion strength for TiN coating in tool applications: a review, J. Adhes. Sci. Technol. 29 (2015) 569–591.
[51] S.J. Bull, Failure mode maps in the thin film scratch adhesion test, Tribol. Int. 30 (1997) 491–498.
[52] S.J. Bull, Failure modes in scratch adhesion testing, Surf. Coat. Technol. 50 (1991) 25–32.
[53] S. Hogmark, S. Jacobson, M. Larsson, Design and evaluation of tribological coatings, Wear 246 (2000) 20–33.
[54] R.Y. Li, Y. Cai, K. Wippermann, W. Lehnert, Corrosion and electrical properties of SS316L materials in the simulated HT-PEFC environment, J. Electrochem. Soc. 165 (2018) C681–C688.
[55] G. Boere, Influence of fluoride on titanium in an acidic environment measured by polarization resistance technique, J. Appl. Biomater. 6 (1995) 283–288.
[56] E. McCafferty, Validation of corrosion rates measured by the Tafel extrapolation method, Corros. Sci. 47 (2005) 3202–3215.
[57] N.D. Nam, D.S. Jo, J.G. Kim, D.H. Yoon, Corrosion protection of CrN/TiN multi-coating for bipolar plate of polymer electrolyte membrane fuel cell, Thin Solid Films 519 (2011) 6787–6791.
[58] L. Chen, J. Hu, X. Zhong, Q. Zhang, Y. Zheng, Z. Zhang, D. Zeng, Corrosion behaviors of Q345R steel at the initial stage in an oxygen-containing aqueous environment: experiment and modeling, Materials 11 (2018) 1462–1481.
[59] M. Songür, H. Çelikkan, F. Gökmeşe, S.A. Şimşek, N.Ş. Altun, M.L. Aksu, Electrochemical corrosion properties of metal alloys used in orthopaedic implants, J. Appl. Electrochem. 39 (2009) 1259–1265.
[60] A. Kahyarian, M. Singer, S. Nesic, Modeling of uniform CO_2 corrosion of mild steel in gas transportation systems: a review, J. Nat. Gas Sci. Eng. 29 (2016) 530–549.
[61] G. Milazzo, Table of standard electrode potentials, J. Electrochem. Soc. 125 (1978) 261–265.
[62] P.R. Roberge, R. Beaudoin, Behavior of the corrosion potential and corrosion current of Cu-Ni alloys under erosion corrosion conditions. Effect of oxygen, J. Appl. Electrochem. 18 (1988) 601–607.
[63] R.A. Antunes, M.C.L. Oliveira, G. Ett, V. Ett, Corrosion of metal bipolar plates for PEM fuel cells: a review, Int. J. Hydrogen Energy 35 (2010) 3632–3647.
[64] F.H. Lu, H.Y. Chen, Characterization of titanium nitride films deposited by cathodic arc plasma technique on copper substrates, Surf. Coat. Technol. 130 (2000) 290–296.
[65] J.F. Marco, A.C. Agudelo, J.R. Gancedo, D. Hanzel, Corrosion resistance of single TiN layers, Ti/TiN bilayers and Ti/TiN/Ti/TiN multilayers on iron under a salt fog spray (Phohesion) test: an evaluation by XPS, Surf. Interface Anal. 27 (1999) 71–75.
[66] Y.H. Cheng, T. Browne, B. Heckerman, Nanocomposite TiSiN coatings deposited by large area filtered arc deposition, J. Vac. Sci. Technol. A 27 (2009) 82–88.
[67] A.C. Agudelo, J.R. Gancedo, J.F. Marco, D. Hanzel, Corrosion resistance of titanium nitride and mixed titanium/titanium nitride coatings on iron in humid SO_2-containing atmospheres, J. Vac. Sci. Technol. A, Vac. Surf. Films (USA) 15 (1997) 3163–3169.
[68] L. Liu, W.J.I. Debenedetti, T. Chopra, S. Gokalp, N. Shafiq, J.-F. Veyan, D. Michalak, R. Hourani, Y.J. Chabal, Morphology and chemical termination of HF-etched Si_3N_4 surfaces, Appl. Phys. Lett. 105 (2014) 261603.
[69] H.J. Grabke, The role of nitrogen in the corrosion of iron and steels, ISIJ Int. 36 (1996) 777–786.
[70] C.L. Chang, J.W. Lee, M.D. Tseng, Microstructure, corrosion and tribological behaviors of TiAlSiN coatings deposited by cathodic arc plasma deposition, Thin Solid Films 517 (2009) 5231–5236.
[71] J. Mertens, E. Finot, O. Heintz, M.-H. Nadal, V. Eyraud, A. Cathelat, G. Legay, E. Bourillot, A. Dereux, Changes in surface stress, morphology and chemical composition of silica and silicon nitride surfaces during the etching by gaseous HF acid, Appl. Surf. Sci. 253 (2007) 5101–5108.
[72] M.C. Li, S.Z. Luo, C.L. Zeng, J.N. Shen, H.C. Lin, C.N. Cao, Corrosion behavior of TiN coated type 316 stainless steel in simulated PEMFC environments, Corros. Sci. 46 (2004) 1369–1380.
[73] S. Balasubramanian, A. Ramadoss, A. Kobayashi, J. Muthirulandi, Nanocomposite Ti-Si-N coatings deposited by reactive dc magnetron sputtering for biomedical applications, J. Am. Ceram. Soc. 95 (2012) 2746–2752.
[74] C. Liu, Q. Bi, A. Leyland, A. Matthews, An electrochemical impedance spectroscopy study of the corrosion behaviour of PVD coated steels in 0.5 N NaCl aqueous solution: Part I. Establishment of equivalent circuits for EIS data modelling, Corros. Sci. 45 (2003) 1243–1256.
[75] C. Liu, Q. Bi, A. Matthews, EIS comparison on corrosion performance of PVD TiN and CrN coated mild steel in 0.5 N NaCl aqueous solution, Corros. Sci. 43 (2001) 1953–1961.
[76] D. Er, G.T.P. Azar, K. Kazmanli, M. Urgen, The corrosion protection ability of TiAlN coatings produced with CA-PVD under superimposed pulse bias, Surf. Coat. Technol. 346 (2018) 1–8.
[77] C. Liu, Q. Bi, A. Leyland, A. Matthews, An electrochemical impedance spectroscopy study of the corrosion behaviour of PVD coated steels in 0.5 N NaCl aqueous solution: Part II.: EIS interpretation of corrosion behaviour, Corros. Sci. 45 (2003) 1257–1273.
[78] J.L. Cui, Z.D. Yao, Y.F. Cui, F.P. Cheng, T. Xiao, H.L. Sun, R.J. Tian, J.C. Sun, Electrochemical properties of tungsten-alloying-modified AISI 430 stainless steel as bipolar plates for PEMFCs used in marine environment, Acta Metall. Sin. 29 (2016) 920–927.
[79] J. Jin, H.J. Liu, D.C. Zheng, Z.X. Zhu, Effects of Mo content on the interfacial contact resistance and corrosion properties of CrN coatings on SS316L as bipolar plates in simulated PEMFCs environment, Int. J. Hydrogen Energy 43 (2018) 10048–10060.
[80] S.P. Mani, B. Rikhari, P. Agilan, N. Rajendran, Evaluation of the corrosion behavior of a TiN- coated 316L SS bipolar plate using dynamic electrochemical impedance spectroscopy, New J. Chem. 42 (2018) 14394–14409.
[81] L. Wang, D.O. Northwood, X. Nie, J. Housden, E. Spain, A. Leyland, A. Matthews, Corrosion properties and contact resistance of TiN, TiAlN and CrN coatings in simulated proton exchange membrane fuel cell environments, J. Power Sources 195 (2010) 3814–3821.
[82] J.W. Yang, S. Esconjauregui, H. Sugime, T. Makaryan, T. Hallam, G.S. Duesberg, J. Robertson, Comparison of carbon nanotube forest growth using AlSi, TiSiN, and TiN as conductive catalyst supports, Phys. Status Solidi B 251 (2014) 2389–2393.
[83] M. Canillas, B. Moreno, M. Carballo-Vila, J.R. Jurado, E. Chinarro, Bulk Ti nitride prepared from rutile TiO_2 for its application as stimulation electrode in neuroscience, Mater. Sci. Eng. C-Mater. 96 (2019) 295–301.
[84] L.X. Wang, J.C. Sun, P.B. Li, J. Sun, Y. Lv, B. Jing, S. Li, S.J. Ji, Z.S. Wen, Molybdenum nitride modified AISI 304 stainless steel bipolar plate for proton exchange membrane fuel cell, Int. J. Hydrogen Energy 37 (2012) 5876–5883.
[85] G.J. Wan, P. Yang, X.J. Shi, M. Wong, H.F. Zhou, N. Huang, P.K. Chu, In vitro investigation of hemocompatibility of hydrophilic SiNx:H films fabricated by plasma-enhanced chemical vapor deposition, Surf. Coat. Technol. 200 (2005) 1945–1949.
[86] D. Blanco, J.L. Viesca, M.T. Mallada, B. Ramajo, R. González, A.H. Battez, Wettability and corrosion of [NTf2] anion-based ionic liquids on steel and PVD (TiN, CrN, ZrN) coatings, Surf. Coat. Technol. 302 (2016) 13–21.